UC Irvine

UC Irvine Electronic Theses and Dissertations

Title

Molecular Dynamics Simulations of Methane Hydrate Dissociation Under Temperature Step and Ramping

Permalink

https://escholarship.org/uc/item/7xz930bq

Author

Cueto Duenas, Dianalaura

Publication Date

2021

Peer reviewed|Thesis/dissertation

eScholarship.org Powered by the California Digital Library
University of California

UNIVERSITY OF CALIFORNIA, IRVINE

Molecular Dynamics Simulations of Methane Hydrate Dissociation Under Temperature Step and Ramping

THESIS

submitted in partial satisfaction of the requirements for the degree of

MASTER OF SCIENCE

in Civil and Environmental Engineering

by

Dianalaura Cueto Duenas

2021

Thesis Committee:

Derek Dunn-Rankin, Ph.D., Advisor, Chair

Yu-Chien Chien, Ph.D., Co-Advisor

Russell Detwiler, Ph.D.

Mohammad Javad Aldolhosseini Qomi, Ph.D.

Penghui Cao, Ph.D.

© 2021 Dianalaura Cueto Duenas

DEDICATION

To my mother, father and grandmother who made possible the impossible.

Table of Contents

List of Figures

List of Tables

Acknowledgements

The conclusion of this thesis wouldn’t have been possible without the efforts and support of many people. I would like to thank Prof. Derek Dunn-Rankin, and Dr. Yu-Chien Chien, for their patience and tolerance during this long and tedious journey, you have taught me more than I can put into words.

Thank you, Prof. Penghui Cao for introducing me to the fascinating world of molecular dynamics, thank you for guiding me when I was overwhelmed and answering even the simple questions that I had.

Also, I would like to thank my committee Prof. Russell Detwiler and Prof. Mohammad Javad Aldolhosseini Qomi.

This research was supported by CONACYT, Ridge to Reef Graduate Training Program, and the University of California, Irvine.

Last but not least, I would like to thank my lovely family, which is my support in everything I do, my friends, who always lend me their ears, and my cat Pimienta.

Abstract of the Thesis

Molecular Dynamics Simulations of Methane Hydrate Dissociation Under Temperature Step and Ramping

by

Dianalaura Cueto Duenas
Master of Science in Civil and Environmental Engineering
University of California, Irvine, 2021
Professor Emeritus Derek Dunn-Rankin, Ph.D., Chair

Methane hydrates are crystalline solids of water that contain methane molecules trapped inside their molecular cavities. Gas hydrates with methane as a guest molecule form Structure I hydrates with a unit cell containing 46 water molecules arranged on 2 small dodecahedral cages and 6 tetra decahedral large cages. An ideal Structure I methane hydrate unit cell contains 8 methane molecules, with one in each cage. Methane molecules are classified according to whether they occupy the large tetra decahedral or the small dodecahedra cells. The influence of occupation and the difference between the behavior of methane release during the dissociation process for the different cage types is the major interest of this work.

To assess and analyze the structure evolution during the dissociation of methane hydrates, a series of molecular dynamics simulations using the Large-scale Atomic/Molecular Massively Parallel Simulator (LAMMPS) is conducted. The dissociation conditions examined include different heating rates at 0.8 TK/s, 4TK/s, 40 TK/s and 400 TK/s, and different temperature increments, ΔT, as steps of 80 K, 85 K, 90 K, 95 K and 100 K above hydrate equilibrium stability conditions for 5 ns. Both simulated systems were first equilibrated at 270 K and 5 MPA.

The potential energy of the system, mean-squared displacement (MSD), and the radial distribution function were analyzed to determine the full process of dissociation, temperature changes,

molecular diffusive behavior, and structure evolution. Temperature step results showed the earliest dissociation starting 50 ps into the simulation at a ΔT of 100 K, while at a ΔT of 80 K, dissociation was not observed. There was not a clear dissociation preference observed between large and small cages, so it appears that the dissociation affects the entire structure uniformly when temperature increases are applied throughout the system rather than transported from a boundary.

Temperature ramping simulations showed that the dissociation temperature increased with an increased heating rate. The mean-squared displacement results for the oxygen atoms in the water molecules at a high heating rate of 400 TK/s showed a similar behavior to that for methane gas. This behavior may be an indicator of fast evaporation for water molecules, while at slower heating rates methane molecules showed much higher MSD values, indicating diffusive behavior. As in the temperature step simulation there were not clear differences in dissociation between large and small cages, which suggests homogeneous dissociation in all cases.

While this study showed that a total occupied hydrate will experience homogeneous dissociation independent of the heating method, (i.e., either gradual temperature increases or constant high temperature exposure), future studies can examine the stability of the hydrate at different occupancies. Additionally, since hydrate is exposed to liquid water in natural settings, it is important for future studies to analyze the impacts of a liquid water interface in the stability and dissociation dynamics of methane hydrate.

CHAPTER 1: INTRODUCTION TO METHANE HYDRATES

1.1 Methane Hydrate Energy and Environmental Disruption Potential

Occurrences of methane hydrates are widespread across the globe, under lakes and oceans at certain temperature and pressure conditions, usually at depths above 300 m (e.g. Arctic) and under 500 m. Hydrates are also found under the permafrost where temperatures are low [1], and there is a wide body of literature mapping methane hydrate reserves.

Gas hydrates are found in different forms in nature. “Pore filling” hydrates form inside the pores of sediments, and they are characterized by their saturation. Hydrate saturation is defined as the percentage of gas in a hydrate per pore volume [2]. Pore filling hydrate has low saturation, typically 10%, depending on the grain size. The greater the grain size, the higher the saturation since there is more pore space to fill with hydrate. Saturation exceeding 90% occurs in some sand sediments [3]. There are also “massive” hydrates, where hydrates form in fractures and grain displacing veins in clay when there is more gas available. In this case saturation depends on the gas supply and it also ranges from 10% to higher as the gas supply is richer.

Methane hydrate resource availability is classified in 3 types. One is the total volume of resource, and another is the Technically Recoverable Resource [TRR], which is the amount of resource that can be technically extracted [e.g depressurization, heat injection]. The third is economically Recoverable Resources [ERR], which is the amount of TRR that is profitable [4].

Global methane hydrate estimates range from tens of thousands to millions of trillion cubic feet (Tcf) of methane gas contained in hydrates. In 2011 Johnson [5], made an assessment of every coastal margin including Polar Regions, and estimated a global TRR of 10^4 Tcf, though no economically recoverable resources were calculated.

Several explorations around the world have been made to estimate hydrate resources occurrence and availability. In 2008, the Bureau of Ocean Energy Management assessed 6700 Tcf in the Gulf of Mexico[6], while the USGS in their North Slope study estimated a total of 85 Tcf of technically recoverable resource [3]. Also, the same year Japan has estimated about 20 Tcf in the Nankai Trough [7].

Occurrence of technically recoverable methane hydrates have also been reported in New Zealand [8], South Korea [9], the Bay of Bengal [10], the South China Sea [11], and the eastern coast of North America [12].

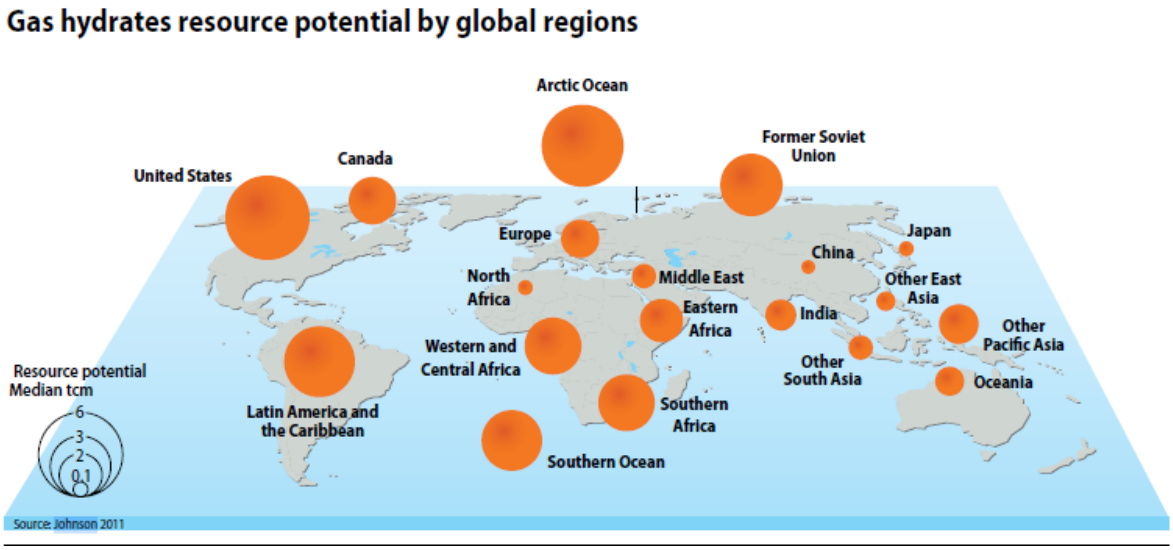

Figure 1. Gas hydrate resource potential by global regions [4-5].

Even though the estimated amount of methane hydrate resource is great, the portion that can be extracted with the current technology is quite limited and even less of that portion can potentially be economically extracted, so is imperative to achieve fundamental methane hydrate dissociation knowledge at every scale to be able to optimize current methane hydrate extraction technologies.

An additional significant impact of methane hydrates is environmental. Methane hydrates are located under the permafrost, near the North poles, and outer continental shelf areas in the deep ocean. When temperature rises and the methane gas is released from permafrost, a greenhouse gas 21 times more harmful than CO_2 based on quantity is released into the atmosphere thus enhancing global warming. Understanding the dissociation of hydrates is an important step in avoiding negative environmental consequences of inadvertent methane release from hydrate.

1.2 Motivation

As mentioned in the prior section, methane hydrates have great potential as an alternative energy source because of their large quantity and occurrence. Moreover, there are different extraction methods that have been investigated and continue developing. Environmental impact is a major consideration of these extraction methods.

One major and long-shot goal of methane hydrate research is to potentially extract the methane as an energy source and at the same time store CO_2 from the atmosphere to form CO_2 hydrate. As one step toward this goal, which is a large-scale process, it is valuable to first understand the principles of how the methane hydrate dissociation/formation process occurs. Understanding, methane hydrates from the smallest scales can be used to escalate the findings to a large scale [13]. It is the small scale understanding of methane hydrates that is the motivation for this thesis research.

1.3 Clathrate Hydrates

Clathrate hydrates are crystalline solids of water, with gas molecules trapped inside their molecular cavities, or cages, that are composed of hydrogen bonded water molecules [14]. Naturally forming methane hydrates occur in outer continental shelf areas under the ocean and under the permafrost

at the poles, where there is an environment of high pressure and low temperature. There is a wealth of published material describing hydrate structure in detail (e.g. [14]) so only the most salient aspects relevant to the simulations in this thesis are repeated briefly here.

Depending on the type of the guest molecule, temperature, and pressure, gas hydrate cages are arranged commonly in 3 different unit cell structures:

1. Structure I (Simple Cubic): The guest molecule has the diameter between 4.2 Å and 6 Å. Structure I consists of 6 large tetrakaidekahedral cages ($5^{12}6^2$) and 2 small pentagonal dodecahedral (5^{12}) cages.
2. Structure II (Face Centered Cubic): Hosts molecules, as single guests, with a diameter (d) under 4.2 Å and 6 Å < d < 7 Å. Structure II consists of 8 large hexakaidecahedral ($5^{12}6^4$) and 16 small pentagonal dodecahedral (5^{12}) cages.
3. Structure H (Hexagonal): Hosts large molecules of 7 Å < d < 9 Å (e.g. iso-pentane or neohexene) when accompanied by smaller molecules such as hydrogen. Structure H consists of 1 large icosahedral ($5^{12}6^8$), 2 medium irregular dodecahedron ($4^3 5^3 6^3$), and 3 small pentagonal dodecahedral (5^{12}) cages.

It is important to note that cavities are prevented from collapsing by the repulsive and attractive forces of guest molecules inside or in neighboring cavities. Moreover, forming a stable hydrate does not require that all of the cavities be filled because the clathrate hydrates are recognized in part by their nonstoichiometric nature [14]. Table 1 summarizes the main hydrate crystal structure properties.

Hydrate Crystal Structure	**I**		**II**		**H**		
Crystal System	Cubic		Cubic		Hexagonal		
Space Group	Pm3n		Fd3m		P6/mmm		
Lattice Description	Primitive		Face centered		Hexagonal		
Cavity	Small	Large	Small	Large	Small	Medium	Large
Description	5^{12}	$5^{12}6^2$	5^{12}	$5^{12}6^4$	5^{12}	$4^3 5^3 6^3$	$5^{12}6^8$
Number of Cavities/unit cell	2	6	16	8	3	2	1
No. of water molecules/cavity	20	24	20	28	20	20	36

Table 1. Structure I, II and H crystal properties [14].

Less common crystals are listed in the Jeffrey's structures from 1967, which identifies hydrate types from I to VII, including type I and II listed in the table above. Structure H had not yet been identified [14-15]. The following paragraph will introduce the properties of the hydrate structure types from Table 1.

Methane Hydrate is usually formed as a structure I hydrate unit cell where methane occupies both large tetrakaidekahedral and small pentagonal dodecahedral cages. Methane can also form Structure II and H hydrates in higher pressure conditions [16–19]. The focus of this study is the fundamental behaviors of the most common methane hydrate Structure I.

As mentioned previously, a hydrate Structure I unit cell is formed by 6 large $5^{12}6^2$ and 2 small 5^{12} cavities. The small pentagonal dodecahedral cavity is known to be the "basic building block" since it is the first cage formed in a hydrate. It is also the most likely structure to from water when it is solidifying. During the dissociation process, it is expected to be the last cage to dissociate or the most stable cage of the structure because of its higher number of bonds to molecules ratio (30/20) compared to other cavities. It is also the least strained.

While the large cage in Structure I is a tetrakaidecahedron, the stability of this cavity is dependent on the guest molecule's shape because of its oblate ellipsoid structure. It also plays the main role in the stability of hydrate Structure I. With a detailed understanding of hydrate Structure I performance and how the key physical properties such as temperature and pressure affect the full dissociation process, this research explores the behavior of small and large cage methane hydrate responses.

1.4 Methane Hydrate Formation

With the knowledge that methane hydrate forms in high pressure and low temperatures in nature, it has been shown that the formation process includes 3 stages: induction, initial rate of consumption, and final rate of consumption [14]. The induction time, also referred to as lag time hydrate nucleation (or onset of massive growth), is the period for the hydrate to be detected at macroscopic scale, including the time for a crystal to nucleate. The nucleation scale is not able to be detected macroscopically, and the process is stochastic, meaning that it is difficult to predict. Being unpredictable and difficult to detect, nucleation is a precursor of the induction time that is not yet well understood. Fortunately, the nucleation time is much shorter than the induction time, so it has relatively little impact on the practical formation process. There are mainly three hypotheses as to how nucleation and initial formation occurs:

- Labile cluster model: Since water clusters form around the guest molecule during the early stages of growth, it was hypothesized that those clusters grow until they achieve a critical radius in what it is called a "prehydrate" [8-9].
- Local structuring nucleation: In this hypothesis it is proposed that the prehydrate is formed because thermal fluctuations cause guest molecules to arrange locally in a structure similar to a hydrate until a critical radius is achieved [21].

- Nucleation at the interface: It is proposed that nucleation occurs in the gas phase of the interface between the gas (guest molecule) and the liquid phase (water molecules); gas molecules move onto the interface where they are adsorbed by water molecules and form clusters in the vapor phase until they reach a critical size [10-11].

After the induction time, hydrate growth accelerates dramatically and it is characterized by a high initial rate of gas consumption, which stabilizes over time (most likely due to limited transport rates) until the final rate of gas consumption at constant temperature and pressure is reached. The end of the clathrate formation is a constant volume process, where the temperature decreases to enhance hydrate formation, and a sudden pressure drop will be observed in the offset point, which depends on initial growth conditions.

Hydrate growth dominates the formation process and is driven mainly by three factors: kinetics of crystal growth, mass transfer of the guest molecules and water molecules, and the heat transfer during the exothermic process of hydrate formation. The initial step of hydrate formation is a stochastic process that is difficult to model and predict. Thus, even though several hypotheses have been proposed, as previously mentioned (and they may all participate to some degree depending on the specific conditions of the system), how exactly hydrates nucleate is not yet confirmed. Consequently, this thesis concentrates on hydrate dissociation which is a more reproducible and definable phenomenon.

1.5 Methane Hydrate Dissociation

Clathrate Hydrate dissociation is an endothermic process because it is necessary to supply heat to break the hydrogen bonds of the cavities to initiate the dissociation. Also, heat transfer from the boundaries causes hydrates to dissociate radially from the edges of the hydrates through the center when trying to eliminate hydrate plugging in a pipe in the oil and gas industry.

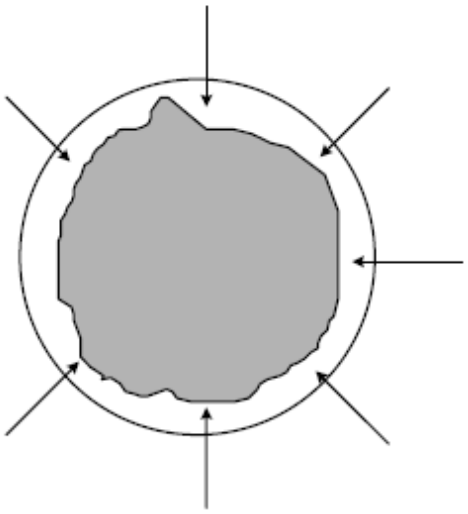

Figure 2. Hydrate Radial Dissociation [14].

Several studies have shown that the dissociation process in hydrates is primarily driven by heat transfer since a thermal gradient occurs from the hydrate zone to the interface [24-25]. The heat is replenished during decomposition, therefore, at the early stages (of decomposition), the hydrate dissociation is controlled by intrinsic kinetics.

Hydrate dissociation does not appear as a sudden trigger or a distinct transition. It is the result of a series of reactions as molecules adapt to the change of surroundings. The full process can be complicated and remains poorly understood. For example, one special condition is when the hydrate is outside of the stability zone but has not yet dissociated even after a prolonged period. This phenomenon is called "self-preservation" and it is a metastable behavior (much like traditional ice remaining intact above freezing temperature). Experiments have also shown that methane hydrates can be metastably preserved for up to 3 weeks [25], which is relevant for gas storage applications of hydrates. Because it begins with a concrete structure, the behavior of hydrate dissociation is appropriate for molecular dynamics (MD) study, which is the subject of

this thesis. The detailed literature review specifically on molecular dynamics studies of methane hydrate dissociation will be presented in Chapter 2.

1.6 Objectives

As outlined above, this research is aiming to understand the influence of cage occupancy of methane hydrates as the methane releases at different heating conditions. Also the system's response to sudden and gradual temperature changes is of interest since some dissociation methods use thermal stimulation as a driving force or a mix of thermal stimulation and depressurization [26]. It is also possible to view depressurization as a uniform change in the temperature condition for dissociation since the hydrate stability temperature depends on pressure. In addition, there is always a thermal component to dissociation since it is an endothermic process requiring heat to drive the phase change.

The thesis is divided into the following chapters:

- CHAPTER 1: Introduction to Methane Hydrates
- CHAPTER 2: Scientific Background of MD for Methane Hydrate Dissociation
- CHAPTER 3: Methane Hydrate Molecular Dynamics, Research Principle, Methods, and System Preparation
- CHAPTER 4: Results and Discussion
- CHAPTER 5: Conclusions and Future of Molecular Dynamics Simulation on Methane Hydrates

CHAPTER 2: SCIENTIFIC BACKGROUND OF MD FOR METHANE HYDRATE DISSOCIATION

2.1 Introduction to Molecular Dynamics (MD)

Molecular Dynamics (MD) is a simulation method for computing the equilibrium and transport properties of a classical many-body system by solving Newton's equations of motion [27] for a specific interatomic potential, with applied initial conditions (IC) and boundary conditions (BC) [28].

Molecular Dynamics simulations are designed to follow the details of a physical process from the molecular level. The current study uses Large-scale Atomic/Molecular Massively Parallel Simulator (LAMMPS) as the tool to study the intermolecular behavior particularly on the full dissociation process while reflecting different strategies. For an in-lab methane hydrate experiment, a hydrate sample is prepared following the principle of the P-T diagram [14]. Then properties of interest, such as temperature and pressure, are monitored at different locations during a time interval as the sample is warmed. In Molecular Dynamics, a sample model is first prepared, and equilibrated applying physical properties (temperature and pressure) to the simulation in a certain time interval. The sample is then warmed numerically. Both experiment and MD simulation require the step of averaging the data in order to observe the mean value from the fluctuation of the raw data. The main difference between the experiment and the simulation is that in the simulation the temperature can be changed instantaneously throughout the sample while in the experiment the heat must be transported into the sample core from the boundary. This difference does not, however, affect the understanding of the local dissociation behavior in the hydrate.

The simplest workflow step concept of a typical MD program follows:

1. Read the parameters that specify the initial conditions of the run (Temperature, Pressure, Density etc.)
2. Initialize the system (Initial positions and velocities)
3. Compute forces on all particles
4. Integrate Newton's equations of motion
5. Compute and output the averages of the measured quantities

2.2 System Set up

Molecular dynamics simulation uses the fundamentals of statistical mechanics to calculate and average the many-body system. To achieve the prediction, the simulation first relies on defining the ensembles and the system. An ensemble is a collection of systems with a set of common macroscopic properties so that each system is in a unique microscopic state at any point in time as determined by its evolution over time [29]. There are 5 statistical ensembles that are commonly employed in MD simulation. They are: microcanonical, canonical, grand canonical, isobaric-isothermal and isoenthalpic-isobaric which are briefly defined as follows.

- The microcanonical ensemble is composed of a collection of systems isolated from any surroundings, all the other 4 ensembles are based on this one. Each system in the microcanonical ensemble is characterized by fixed particle number N, volume V, and total energy E and thus is also called an NVE ensemble.
- The canonical ensemble is described as an NVE system surrounded by a heat bath and permitting an exchange of energy. Its thermodynamic control variables are constant particle number N, constant volume V, and constant temperature T, which characterize a

system in thermal contact with an infinite heat source. It is also referred to as the NVT ensemble.

- The isobaric-isothermal ensemble can be described as an NVT ensemble with the pressure fixed, which means the volume of the system is allowed to fluctuate. Its thermodynamic control variables are constant particle number N, constant pressure P, and constant temperature T. It is also referred to as the NPT ensemble.

Other ensembles are the Isobaric-Isoenthalpic ensemble, which is constant particle number N, constant pressure P and constant enthalpy H. The Grand Canonical ensemble has a fixed chemical potential μ, constant volume V and constant temperature T.

Beside the choice of the ensemble for computing hydrate, the boundary conditions are also an important aspect to identify the detailed physical constraints in LAMMPS software. There are 4 types of boundary conditions that can be used for modeling.

- Periodic: The box (simulation domain) is periodic, and the atoms or particles can interact across the boundary. They can exit one end of the box and re-enter the other end.
- Non-periodic and fixed: One face of the box is fixed.
- Non-periodic and shrink-wrapped: The positions of the face are set to encompass the atoms in that dimension, no matter how far they move.
- Non-periodic and shrink-wrapped with minimum value: Shrink-wrapping occurs such as, when you want to leave room on one side of the simulation box to model the evaporation of atoms from a surface, but is bounded by a value specific value [30].

2.3 Forcefield Models for H_2O and CH_4

2.3.1 Background of Interatomic Potential

Once the system (thermodynamic ensemble) and boundary conditions are determined, the next step is to calculate the energy of every particle in the system. The interatomic potential is a mathematical function to calculate the interactions between each particle. The sum of all such individual potential comprises the system potential energy.

In molecular dynamics simulation, it is important to optimize the computational resources needed for its calculations since it can be both time consuming and expensive. The most intensive calculations are the interatomic forces of the system, and the results of the simulation will be dependent on the type of interatomic potential model that is used. Therefore, the choice of the appropriate model that is both accurate and non-computationally demanding is important for considering their characteristics. This is because one molecule can have several interatomic potential models, and each model is designed to describe the interatomic forces depending more effectively on the simulation's conditions. There are also cases where we are not interested in some properties of the molecules, and we can use a simpler model to reduce the computational resources [27].

Interatomic potentials are classified as parametric or non-parametric with respect to sub-types. Parametric potentials are models based in several fixed parameters and they have the following sub-types.

- Repulsive Potentials: used for short interatomic distance interactions and are best described by Coulomb Potentials [31].

- Many-Body Potentials: used to describe more than two particle interactions and are commonly used for characterizing metals [32].
- Forcefields: used to describe the interactions between particles of ~10^8 units [33].
- Pair Potentials: used to describes the pairwise interaction forces between two particles. The most widely used pair potential model is the Lennard-Jones potential. Both the water and methane potential models used in the current work are based on this model. Hence, for a better understanding, a detailed description of the Lennard-Jones potential will follow.

The Lennard-Jones Potential was developed by John Edward Lennard-Jones [34], and it describes the interaction between to non-bonding particles based on their separation distance and accounts for both attractive and repulsive forces in which the model is divided.

The Lennard Jones Potential is given by the following mathematical model:

$$V(r) = 4 \in \left[\left(\frac{\sigma}{r}\right)^{12} - \left(\frac{\sigma}{r}\right)^{6}\right]$$

Where:

$V(r)$ is the interatomic potential between the two particles

$\in$ is the interatomic potential well depth

σ is the distance in which the interatomic potential is zero

r is the distance between the two particles

The attractive forces are described by $\left(\frac{\sigma}{r}\right)^{6}$, based on the Van der Waals forces, while the repulsive forces are described by $\left(\frac{\sigma}{r}\right)^{12}$, which is calculated as the square of the attractive forces, and are

related to the Pauli Exclusion Principle [35-36]. Other pair potential models include the Morse potential and the Buckingham potential.

Pair-potentials are also classified between short-range interactions, which describes interactions of atoms only when they are close to the radius of potential minimum energy, and long-range interaction where r is many times larger than the r associated with minimum interaction potential. It is important to note that a long-range interaction potential is simpler and less computationally intensive than a short-range one. In molecular dynamics simulations, a cutoff distance r_c is added to pair potential potentials with the purpose of limiting the evaluation of interactions between the pair of atoms; r_c is usually chosen to be less than half of the diameter of the periodic box.

Non-Parametric potentials are based on mathematical optimization methods, and the most recent machine-learning methods, including linear regression and neural networks among other algorithms to calculate an interatomic potential model [36].

Interatomic potential models are also classified according to how they describe interactions between atoms in molecules. They are categorized as atomistic potentials and coarse-grain models. Atomistic potentials describe the interaction of each individual atom in a molecule while coarse-grain models describe the molecules as pseudo-atoms approximating the interaction values as a group. Coarse grain models have fewer degrees of freedom leading to a shorter simulation times but also to less accuracy for some molecular properties depending on the specific model [37]

2.3.2 Water Forcefield

2.3.2.1 Introduction

This section introduces the classifications of the types of water interaction potential models. The current study is emphasizing the TIP4P water models and the logic behind the selection of intermolecular forces. They are based in Lennard-Jones (mentioned above in 2.3.1) and Coulombic interactions [31].

Water models are classified based on the number of interaction sites, the intramolecular characteristics (e.g., if it contains dummy particle or not), and whether the model is polarizable or not. All of them are atomistic.

Water models can be flexible or rigid according to their intramolecular characteristics. Rigid water models describe the molecule according to its true geometry. For example, an isolated water molecule has an angle between hydrogens of 104.52◦, so the rigid model has these angles while some flexible models will have an angle of 109.47◦. Because the rigid model relies on non-bonded interactions, while flexible models account for bond stretching, angles bending and vibrations, the rigid water model is faster to calculate [30].

There are 3 main water models classified according to the number of interaction sites 3, 4 and 5.

The 3-site water model takes account of the interactions of each atom in a water molecule and thus three interaction sites. Examples of 3-sites models are rigid TIP3P [38] and flexible SPC/E [39] among others.

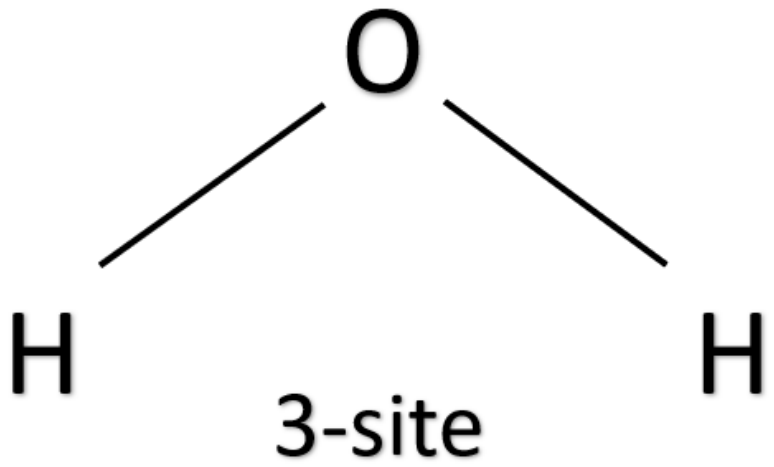

Figure 3. 3-Site Water Molecule Model.

The 4-site model has 4 interaction sites. Apart from the hydrogen and the oxygen there is a fourth "dummy" [M] atom with a negative charge added in the bisector of the H-O-H angle for improving the electrostatic distribution. Figure 4 is an examples of 4-site models included in the rigid TIP4P [38] variations and flexible SPC [39-40] models among others.

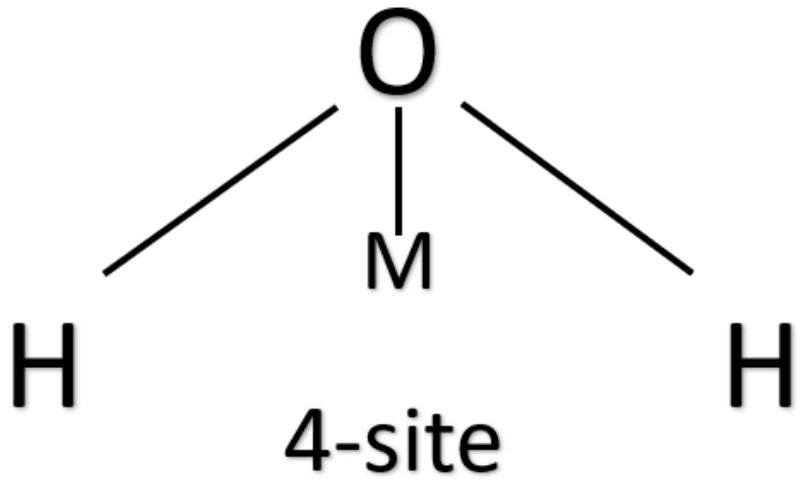

Figure 4. 4-Site Water Molecule Model.

The 5-site model adds two “dummy” molecules that represent the lone pairs of oxygen. It has a high computational cost (in time and processor) compared to the 3-site and 4-site models, so it is less commonly used. Figure 5 is an example of the 5-site model included in the rigid TIP5P model [38].

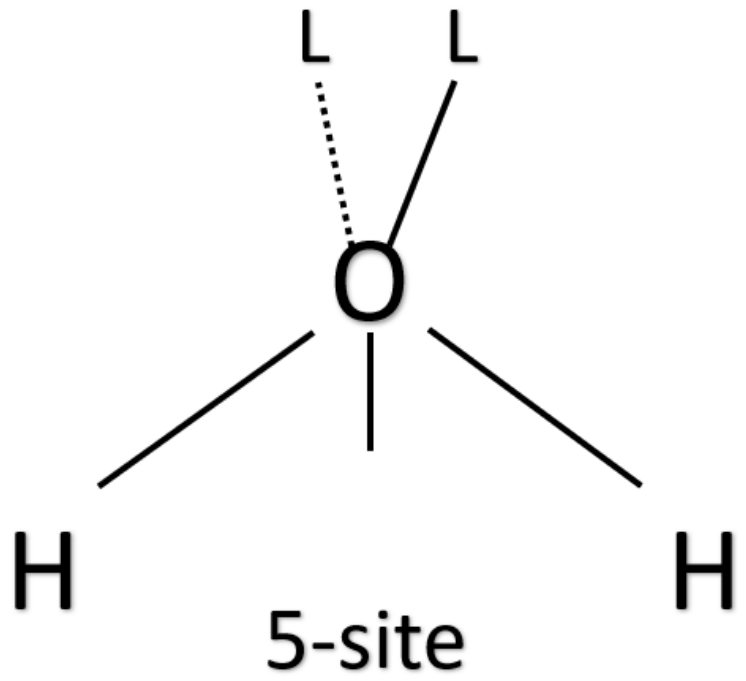

Figure 5. 5-Site Water Molecule Model.

A TIP4P water force field was used in the molecular dynamics’ simulations performed in this study. For the purpose of validating the TIP4P forcefield, a literature review and water dimer simulations were performed on LAAMPS.

2.3.2.2 Water Forcefield Evaluation

As previously mentioned, there are several water forcefield models defined and the choice forcefield would impact the simulation results of a hydrate since it is mostly conformed by water molecules. Therefore, identifying the appropriate forcefield would help to get accurate results for

the properties of interest, which in this case is to obtain reliable density values and melting temperature behavior, particularly as regards the dissociation of hydrate cages. First, we need to know if a 1-site, 2-site, 3-site, 4-site, or 5-site water forcefield is better to describe the desired melting temperature and density.

In 1983 Jorgensen et. al [41] performed classical Monte Carlo simulations of six different water forcefields to describe a water dimer, Bernal-Fowler, SPC, ST2, TIPS2, TIP3P and TIP4P. They compared the results with experimental data. They found that the computed densities were acceptable for all the forcefields except the Bernal-Fowler with 18% disagreement from experimental data. The most accurate results were obtained by the TIP3P and TIP4P forcefield with 2% and 0% error respectively. Note that in the case of this thesis study the goal is not to predict the melting point precisely but to ensure a low melting point so that hydrate dissociation will be obtained.

Later in 2006, the simulation of the melting point for ice by Garcia Fernandez et al.[42] was determined from molecular dynamics simulations of boxes containing a liquid water and ice interface using 7 different water forcefields: SPC/E, TIP4P, TIP4P-Ew, TIP4P/ice, TIP4P/2005, TIP5P and TIP5P-E. It was found that the lowest melting point was calculated using the original TIP4P.

2.3.2.3 TIP4P and TIP4P/2005 Water Forcefield Simulations

In order to verify the prediction of density calculation from different options of forcefield, TIP4P and TIP4P/2005 molecular dynamics simulation of liquid water at constant pressure of 1 bar and temperature 298 K were performed. A system with 360 water molecules was modeled for 80000 cycles, and each cycle is 2 femtoseconds. Works from Jorgensen et al [43] and Abascal et al [44] with the same amount of water molecules undergoing the same T and P, but with TIP4P and

TIPTP/2005 respectively are used for comparison [43-44]. The experimental result from Guillot is also used for verification [45] with the same conditions.

The analyzed density result is averaged every 80 cycles. The standard error (SE) was used to calculate a statistically consistent value. Density results from the experiment in [45] at 1 bar and 298 K was $\rho_{exp} = 0.9971\, {}^{g}/_{cm^3}$,and the simulated density of this work for TIP4P was $\rho_{TIP4P} = 1.0279\, {}^{g}/_{cm^3}$ with SE=0.0004 in which the relative error is 3.09 % (to experimental value). The density results for TIP4P/2005 were $\rho_{TIP4P-2005} = 0.9883\, {}^{g}/_{cm^3}$ with SE=0.0004 and the relative error is 0.887% which is smaller than for the results predicted with the TIP4P forcefield. The simulated results are consistent with Abascal et al [44] where TIP4P/2005 had a better performance for density calculation than TIP4P which also resulted in a larger value than the experimental value.

FORCEFIELD	STANDARD ERROR	DENSITY $[{}^{g}/_{cm^3}]$	RELATIVE ERROR
TIP4P	0.0004	1.0279	3.09%
TIP4P-2005	0.0004	0.9883	0.88%
EXP. [44]		0.9971	

Table 2. Results for density of liquid water simulations at 298 K and 1 bar using TIP4P and TIP4P-2005 water forcefield.

To conclude, TIP4P/2005 is better for density prediction, while TIP4P overestimates density. This is consistent with Abascal et al [44], which stated that TIP4P overestimates thermodynamic properties and TIP4P calculates an accurate value.

Even though the above analysis is discussed only for density prediction, the TIP4P water forcefield for methane hydrates simulation is chosen because this research is focused on dissociation

behavior and starting with TIP4P can reduce simulation time without adversely affecting dissociation dynamics. Although, it underestimates the melting temperature, the development of the thermodynamical properties is not the center piece of this work, which is instead to observe the trend without having a significant difference with experimental values.

2.3.3 Methane Forcefield

As mentioned in 2.3.1, the interactions between molecules of the interatomic potential have two categories, atomistic potentials, and coarse-grain models. For the methane molecule, the interatomic atomistic and coarse-grained models are in common use. Coarse-grained methane models are more often used when the system includes more complex molecules other than methane or when the system is large. This model is used to reduce computational time. Examples of this models include Optimized Potentials for Liquid Simulations United Atom (OPLS-UA) and, Transferable Potential or Phase Equilibria-United Atom (TraPPE-UA) forcefields.

The TraPPE-UA (Transferable Potentials or Phase Equilibria- United Atom) potential model , which was developed in 1998 in the University of Michigan, [46] is parametrized from Lennard-Jones and Coulombic potentials, like water models. It is a coarse-grained model used in large organic compounds. This model is simplifying carbon and hydrogen interactions by treating them as pseudo-atoms or single interactions sites. Pseudo-atoms in TraPPE–UA include CH_4, CH_3, CH_2, CH and C.

Atomistic models are used in systems where methane is the main molecule of interest. All atom interactions need to be regarded individually. Examples of atomistic models include Optimized Potentials for Liquid Simulations (OPLS) [47] and Siepmann, Karaborni and Smit (SKS) [48], two kinds of forcefield for methane. Since our system's main interest is methane hydrate structure

formed by water molecules, simulation time is reduced by simplifying methane interactions using TraPPE-UA.

2.3.3.1 Methane Simulations

As previously mentioned, forcefields can be atomistic in which each bond of the atom interaction is individually taken into account or it can be simplified to one-site in which all the interactions are averaged and distributed in one point which describes the whole molecule. To reduce the simulation times, the single site methane forcefield TraPPE-UA was selected. Before it is used in methane hydrate simulations, similar to the water forcefield section in 2.3.2.3, the forcefield was tested to calculate methane volume at STP and critical temperature. Results were compared with data from the U.S Chamber of Commerce [49] and Teja et al [50].

The TraPPE-UA was tested with both 4,000 and 12,000 simplified methane molecules (pseudo atoms) at constant pressure and temperature at 1 bar and 298 K respectively. The simulations ran for 10,000 cycles in the NVT ensemble and the coefficient of variation (CV) at every 1,000 cycles was used as a standard to analyze volume values. Experimental volume values were calculated for 4,000 and 12,000 methane molecules from density of methane at 1 bar and 298 K from the U.S Chamber of Commerce [49]. A volume of $164{,}000{,}000\ \dot{A}^3$ was obtained for 4,000 methane pseudo atoms with a CV of 0.16% and the relative error to the literature is 0.79%. For 12,000 methane molecules a volume of $488{,}100{,}000\ \dot{A}^3$ was calculated with a CV of 0.09% and the relative error is 0.43% with the literature value.

No. of Molecules	Temperature [K]	Pressure [bar]	Volume [$\dot{A}^3$]	Experimental Results [49] [$\dot{A}^3$]	Relative Error
4000	298	1	164,000,000	162,699,981.6	0.79%
12000			486,000,000	488,100,000	0.43%

Table 3. Results for volume calculations of 4,000 and 12,000 methane molecules using TraPPE UA forcefield.

Methane gas simulations showed a good agreement with literature values with a difference lower than ~1%. Simulations also showed less variability at a higher number of molecules which means that simulations of larger systems are more reliable than smaller systems at the same number of cycles, which could indicate that more simulations cycles are needed to get a more accurate value for smaller systems.

To calculate the critical temperature, 4,000 and 12,000 methane pseudo atoms were simulated at 1 bar and a temperature ramping from 60 K to 350 K. The simulations ran for 100,000 cycles in the NVT ensemble. The output was averaged every 2,000 cycles. Initial volume configurations were calculated for 4,000 and 12,000 pseudo atoms from the liquid density of methane. Figure 6 show a spline shape to describe the change of volume over the change in temperature. To determine the critical temperature, a second derivative analysis over the curve was performed using MATLAB. Results are shown in Table 4. A critical temperature of 191.39 was obtained with a relative error of 0.41% compared to Teja et al [50] for 4,000 pseudo atoms while a critical temperature of 189.98 K was obtained for 12,000 pseudo atoms with a relative error of 0.32%, consistent with previous volume simulations.

In summary, given good agreement values for volume and temperature it is reasonable to use TraPPE-UA to decrease the simulation time.

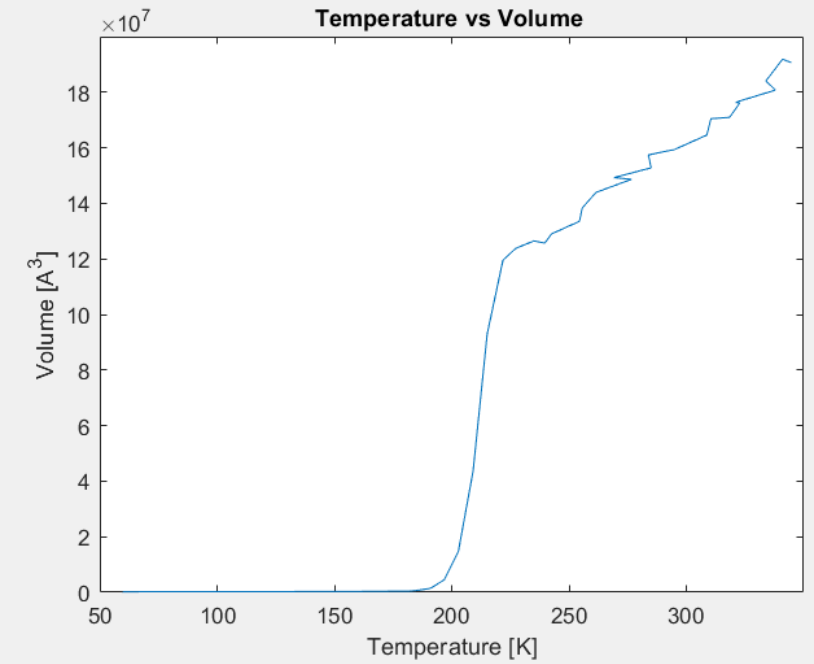

Figure 6. Change in volume of methane during an increase of temperature from 60K to 350K.

No. of Molecules	Initial Temperature [K]	Final Temperature [K]	Pressure [bar]	Critical Temperature [K]	Teja et al [49][K]	Relative Error
4000	60	350	1	191.39	190.6	0.41%
12000				189.98		0.32%

Table 4. Results of simulations to calculate the critical temperature of methane.

2.4 Integration of Newton's Equations of Motion and Molecular Dynamics Algorithms

2.4.1 Verlet Algorithm

In molecular dynamics, the most used time integration algorithm is the Verlet Algorithm, integrates Newton's equation of motion in the NVE ensemble

$$m_i \frac{d^2 \mathbf{r}_i}{dt^2} = -\sum_{j \neq i} \nabla_i U(|\mathbf{r}_i - \mathbf{r}_j|).$$

The basic idea is to write two third-order Taylor expansions, for the positions, one forward and one backward in time [51].

The steps to obtain the velocity of Verlet, which is the most commonly used algorithm in MD, are as follows:

$$\begin{aligned}
\mathbf{r}_i(t+\delta t) &= \mathbf{r}_i(t) + \mathbf{v}_i(t)\delta t + \frac{\mathbf{f}_i(t)}{2m_i}\delta t^2 \\
\mathbf{v}_i(t+\delta t/2) &= \mathbf{v}_i(t) + \frac{\delta t}{2}\frac{\mathbf{f}_i(t)}{m_i} \\
\mathbf{f}_i(t+\delta t) &= \mathbf{f}_i(\mathbf{r}_i(t+\delta t)) \\
\mathbf{v}_i(t+\delta t) &= \mathbf{v}_i(t+\delta t/2) + \frac{\delta t}{2}\frac{\mathbf{f}_i(t+\delta t)}{m_i}
\end{aligned}$$

Where r_i, v_i and f_i represent the position, velocity, and force of the $i-th$ particle.

2.4.2 Nose-Hoover Thermostat and Barostat.

In order to control the temperature in a molecular dynamic simulation, it is necessary to use an algorithm that represents a thermostat. The thermostat allows the MD simulation to achieve a constant temperature process toward the realistic condition. The most used is the Nose-Hoover thermostat, and this algorithm can also be used as barostat. The Nose-Hoover algorithm is an integration in the NVT ensemble, in which a dynamical variable representing friction ς is added to the velocity Verlet algorithm, and allows a time averaged value of the temperature or the pressure [51].

$$
\begin{aligned}
m_i \frac{d^2 \mathbf{r}_i}{dt^2} &= \mathbf{f}_i - \zeta m_i \mathbf{v}_i \\
\frac{d\zeta(t)}{dt} &= \frac{1}{Q}\left[\sum_{i=1}^{N} m_i \frac{\mathbf{v}_i^2}{2} - \frac{3N+1}{2} k_B T\right],
\end{aligned}
$$

The steps to obtain the Nose-Hoover integration are as follows

$$
\begin{aligned}
\mathbf{r}_i(t+\delta t) &= \mathbf{r}_i(t) + \mathbf{v}_i(t)\delta t + \left(\frac{\mathbf{f}_i(t)}{m_i} - \zeta(t)\mathbf{v}_i(t)\right)\frac{\delta t^2}{2} \\
\mathbf{v}_i(t+\delta t/2) &= \mathbf{v}_i(t) + \frac{\delta t}{2}\left(\frac{\mathbf{f}_i(t)}{m_i} - \zeta(t)\mathbf{v}_i(t)\right) \\
\mathbf{f}_i(t+\delta t) &= \mathbf{f}_i(\mathbf{r}_i(t+\delta t)) \\
\zeta(t+\delta t/2) &= \zeta(t) + \frac{\delta t}{2Q}\left[\sum_{i=1}^{N} m_i \frac{\mathbf{v}_i(t)^2}{2} - \frac{3N+1}{2} k_B T\right].
\end{aligned}
$$

Where r_i, v_i and f_i represent the position, velocity, and force of the $i-th$ particle and ζ is the variable representing friction.

2.5 Molecular Dynamics Simulations of Methane Hydrate Dissociation

Prior molecular-scale methane dissociation studies have brought to light the understanding of thermodynamic properties and have helped understanding on the mechanisms as well as kinetics of methane hydrate dissociation.

Methane hydrate dissociation was described as a two-stage process by Ding et al. [52]. They simulated a methane hydrate system with a constant pressure of 30 bar and temperatures at 315, 320 and 325 K to analyze dissociation. The first stage of dissociation consisted in the increase of diffusive behavior for the host water molecules until the lattice structure of water cages broke. The second stage consisted in the escape of methane molecules from the water cages. Similar results were found by Iwai et al [53], but instead of bringing the system to a sudden temperature change, they gradually increased temperature above equilibrium at different heating rates. They also

observed a two-stage dissociation process where water cages broke down first, and then methane escaped.

Methane hydrate cage occupancy effects were studied by Myshakin et al. [54]. They showed that an increase in the number of empty cages decreased stability considerably, speeding dissociation and decreasing melting temperature, and thus decomposition rate was found to be highly dependent on the hydration number.

Several methane hydrate dissociation molecular dynamics simulations were performed by Kondori et al. [55] to study impacts of temperature, pressure, and cage occupancy. They found that methane hydrates were less stable at higher temperatures and more stable at higher pressures. They also noticed a destabilization effect with decreasing cage occupancy, as previously reported by [54]. They also studied the effect of methanol as inhibitor and found that it decreased dissociation time. The molecular simulation study presented in this thesis looks to enrich insights in previous findings and give a new perspective on methane hydrate dissociation.

CHAPTER 3: METHANE HYDRATE MOLECULAR DYNAMICS RESEARCH PRINCIPLES, METHODS AND SYSTEM PREPARATION

This chapter introduces the molecular dynamics simulation tool, Large-scale Atomic/Molecular Massively Parallel Simulator (LAAMPS), that is being used for this research. The chapter provides the details of methodology, preparing the system and steps involved in conducting this study with LAAMPS. A scheme describing the methodology for all simulations is shown in Figure 7.

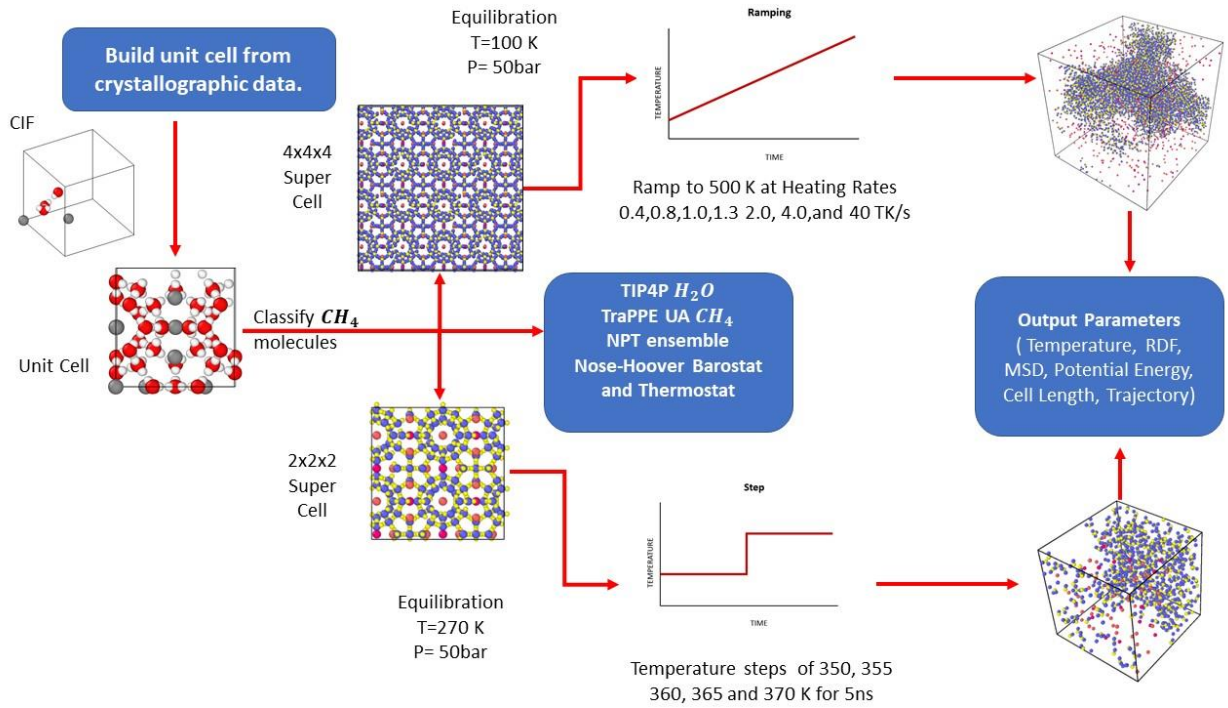

Figure 7. Methane hydrate molecular dynamics simulation methodology diagram.

3.1 Software

3.1.1 Large-scale Atomic/Molecular Massively Parallel Simulator (LAAMPS)

LAAMPS, is a Large-scale Atomic/Molecular Massively Parallel Simulator which was developed at Sandia National Laboratories. It is a classical molecular dynamics code for modeling different

ensembles of particles in the different states of matter as well as macroscopic systems by using diverse forcefields and boundary conditions. The model can be in either 3D or 2D for up to billions of particles. The code was designed to be run on parallel computers for runtime efficiency, but it can also be run on desktops and laptops. LAAMPS is widely used to simulate hydrate systems [56], since it allows easy modifications to forcefield parameters, atom types and other properties that are important for a three phase system such as methane hydrates[30, 53].

3.1.2 Visual Molecular Dynamics (VMD)

VMD stands for Visual Molecular Dynamics. It is a visualization software, developed at the University of Illinois at Urbana-Champaign, for viewing and analyzing the raw data results of the particle systems from molecular dynamics simulations. VMD can be used to animate and analyze particle trajectories as well as for providing various rendering methods for images and animations. For this work VMD was used for visualizing purpose and analysis, including classifying atom types of the initial methane hydrate system [57]. It also allows for communication between the MD simulation and the desired plug-ins, which were developed for the field of interest, for example: in biology to visualize proteins.

3.1.3 Open Visualization Tool (OVITO)

OVITO is scientific visualization and analysis software specifically designed for many-body systems, and it was developed by OVITO GmbH founded by the original developer Dr. Alexander Stukowski. It is useful to get data particularly on material properties at an atomistic level, such as symmetry, strain, dislocation and common neighbor analysis, among others [58].

3.2 Methane Hydrate Preparation.

In this section, a description of how the hydrate system was built for simulations as well as the parameters for water and methane forcefield and initial conditions for the two types of simulations, temperature ramping and step, will be explained in detail.

3.2.1 System Set Up

The initial geometry of the methane hydrate is built using AVOGADRO [59], a cross-platform molecular editor. The overall steps are as follows:

1. An existing hydrate Crystallographic Information File (CIF) (Figure 8) [60], was modified to eliminate the hydrogens to reach 92 hydrogen molecules for a methane hydrate unit cell using AVOGADRO. This step can either be achieved with PDB (Protein Data Bank) file by first converting it to PDB or in AVOGADRO and then converting it after.
2. Multiply the modified hydrate CIF file using AVOGADRO to get the Unit Cell (Figure 9).
3. Export the PDB file.
4. Import the data in VMD
5. Edit PDB file to add angles, mass, and molecular data.
6. Convert to DATA file readable to LAAMPS.
7. Multiply Unit Cell in LAAMPS to create DATA file at the desirable Supercell size (multiples of the unit cell, e.g. 2x2x2).

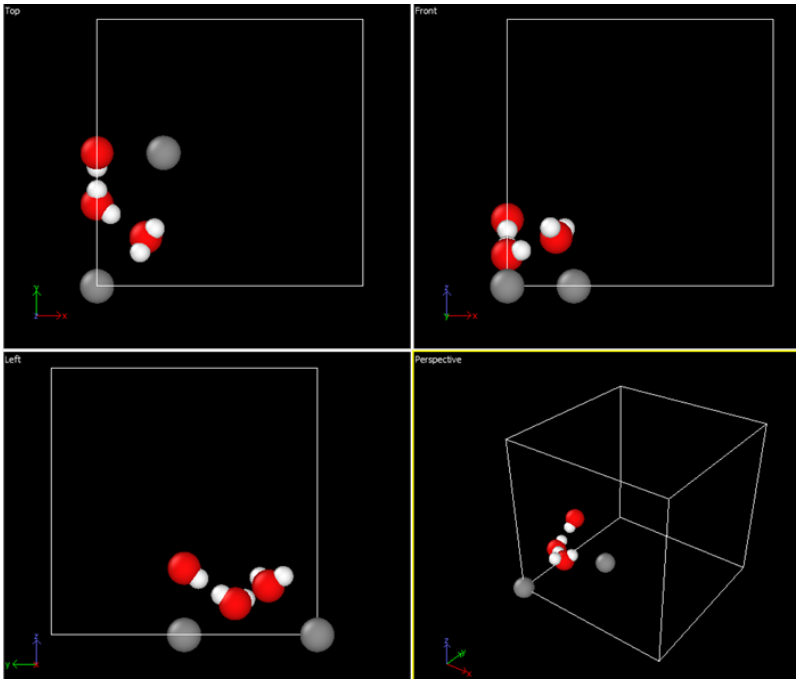

Figure 8. Methane hydrate Crystallographic Information File (CIF).

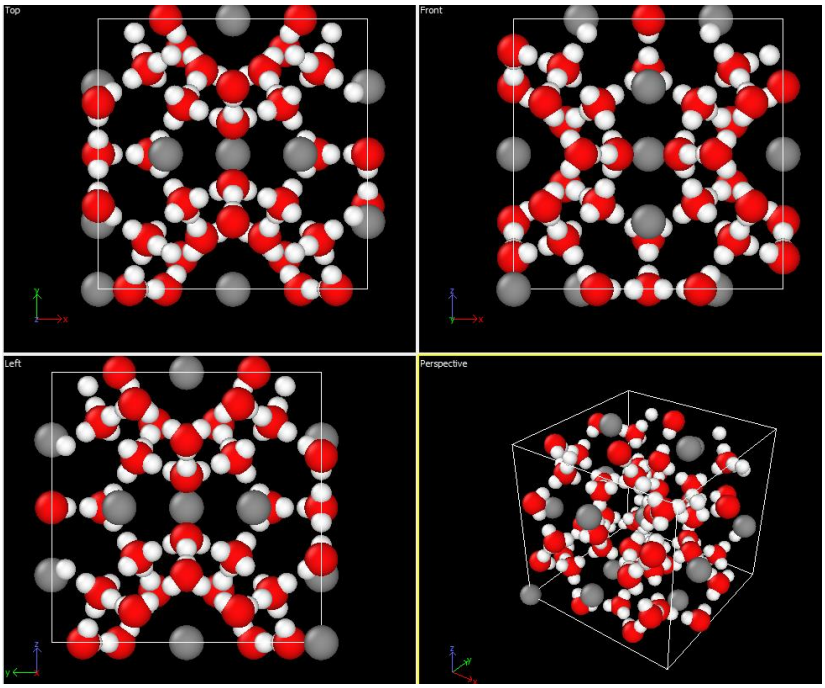

Figure 9. Methane hydrate unit cell from different viewpoints, top, front, left and perspective using OVITO.

3.2.2 Forcefield Parameters

For the methane hydrate forcefield a cutoff distance of 8.5 $\dot{A}$ as well as the following parameters were included using TIP4P and TraPPE forcefield.

Molecule	$\sigma\,(\dot{A})$	$\epsilon\,(^{Kcal}/_{mol})$
H_2O	3.1536	0.1550
CH_4	3.73	0.2941

Table 5. Methane hydrate forcefield parameters for water and methane molecules.

3.2.3 Methane Hydrate System Equilibration

Before the start of the actual simulation the hydrate system needs to be equilibrated at a stable condition, so the overall system is maintained at a coherent state with our desired initial phases. Since this work is performed in the NPT ensemble we chose a temperature and pressure in which methane hydrate is stable for molecular dynamics simulations. Note that the system scale is dramatically smaller than experimental scale, and so the hydrate stability conditions are different for molecular dynamics simulations than occurs in a macroscopical physical system.

Figure 10 presents the methane hydrate equilibrium curve calculated by Kvamme in 2019 [61]. It shows that at a temperature of 270 K methane hydrate is stable at pressures above 20 bar. For a molecular scale a methane hydrate is expected to be stable at 270 K with a pressure much higher than 20 bar. Several molecular dynamics studies on methane hydrates have used a pressure of 50 bar at a temperature of 270 K, thus we chose this equilibrium condition for the temperature step cases [53, 62].

For temperature ramping equilibrium conditions, a pressure and temperature of 50 bar and 100K were used since we aimed to gradually increase temperature, and a lower initial temperature provides the possibility of a higher range of heating rates.

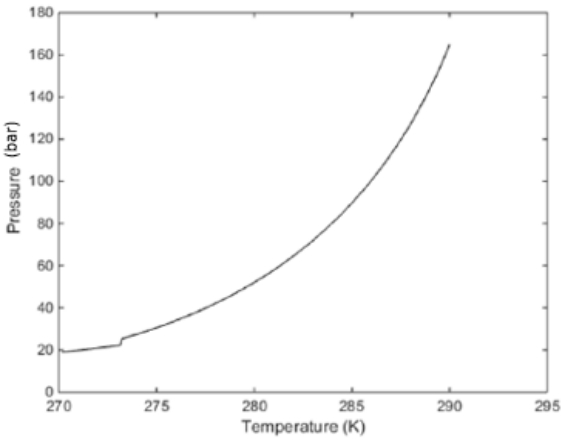

Figure 10. Methane hydrate equilibrium curve.

3.2.4 Simulation Conditions

As described above, the hydrate is equilibrated at 50 bar and 100 K which is the initial condition for the simulated dissociation process. The simulation is then set up for a set of 7 different ramping conditions at various heating rates. The schematic temperature with a constant ramp rate is showing in Table 6, and initial and final temperature are also marked.

The system uses a 4x4x4 fully occupied methane hydrate unit cell for best results and comparison. The system is set with periodic boundary conditions in all directions and in the NPT ensemble at constant pressure of 50 bar and increasing temperature at the different heating rates shown in Table 7. The same forcefields were used for all simulations, TIP4P for water molecules and TraPPE UA to describe methane interactions. A snapshot of the methane hydrate system used in the simulations is shown in figure 11.

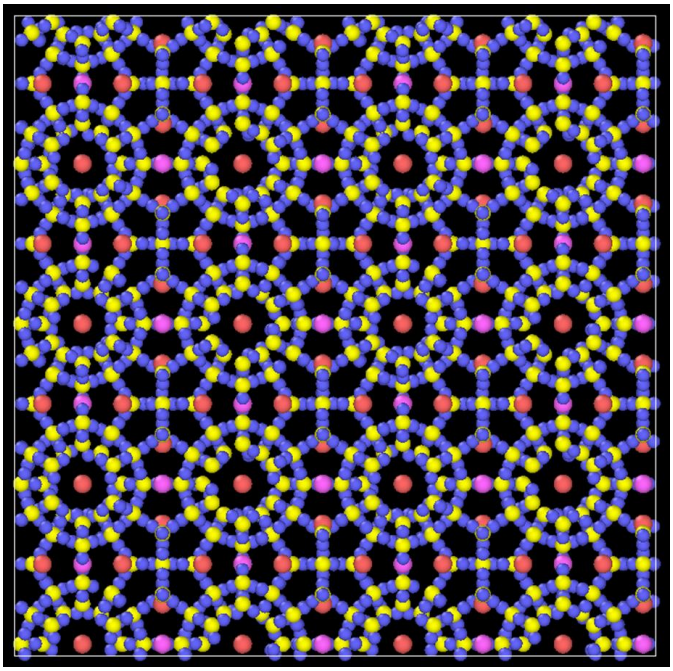

Figure 11. 4x4x4 fully occupied methane hydrate unit cell. Methane molecules are shown in red for methane in large cages and bright pink in small cages, hydrogen atoms are shown in blue and oxygen atoms in yellow.

The simulated time, which represents the time it took the system to increase from the initial temperature of 100K and reach the final temperature of 500 K, is recorded in Table 6. This does not represent dissociation time but the simulated molecular interaction time. The duration is different for each condition because it was the parameter used to control the heating rate.

Simulated Time	Pressure [bar/ATM]	Initial Temp. [K]	Final Temp. [K]	Heat Rate [Tk/s]
1ns	50	100	500	0.4
0.5ns	50	100	500	0.8
0.4ns	50	100	500	1
0.3ns	50	100	500	1.3
0.2ns	50	100	500	2
.1ns	50	100	500	4
.01ns	50	100	500	40

Table 6. Temperature ramping conditions with time schematic with an initial temperature of 100K and final temperature of 500K.

Similarly to ramping, a simulation was conducted at different temperature step size to understand how the temperature change along the time affects the dissociation. A set of 5 different simulations at 5 different temperature steps were performed. Table 7 shows the concept of the step temperature applied for methane hydrate in these experiments along the timeline with initial and final conditions. The system used for the step temperature change is a 2x2x2 fully occupied methane hydrate unit cell since all the simulated times were 5ns, which is larger than the simulated times used for temperature ramping simulations, and we wanted to further decrease computational load and thus we decreased the system size.

The temperature step sizes, with a $\Delta \boldsymbol{T}$ of 80 K, 85 K, 90 K, 95 K and 100 K, are applied on the unit cell with an initial temperature of 270K, which is the stability temperature of methane hydrate at 50 bars (5 MPA). The initial temperature is different from ramping cases because in this case,

temperature is increased instantly and thus dissociation is obtained at a temperature lower than 500K.

Simulated Time	Pressure [bar/ATM]	Initial Temp. [K]	Final Temp [K]	ΔT[K]
5ns	50	270	350	80
5ns	50	270	355	85
5ns	50	270	360	90
5ns	50	270	365	95
5ns	50	270	370	100

Table 7. Temperature step simulation conditions.

With this one step temperature increment directly to the region where methane hydrate dissociates, the final temperature reflects the step of 350 K, 355 K, 360 K, and 370 K respectively. The simulation was performed in the NPT ensemble and the simulation of the molecular dynamics period is for 5ns for all the cases. The test conditions described above are shown in Table 8. Water molecule interactions were described using TIP4P and methane molecules using TraPPE UA as in the previously described simulations. A snapshot of the methane hydrate system used in the simulations is shown in figure 12.

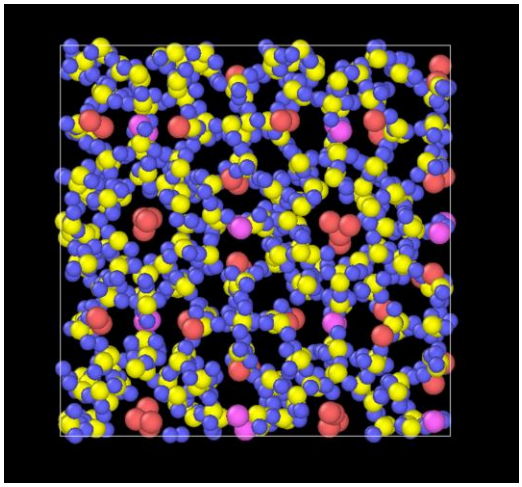

Figure 12. 2x2x2 methane hydrate system used in the temperature step simulations. Methane molecules are shown in red for methane in large cages and bright pink in small cages, hydrogen atoms are shown in blue and oxygen atoms in yellow.

3.3 Analysis Measures and Methods

There are different methods and criteria to determine the dissociation temperature. This work uses potential energy, mean squared displacement (MSD), and change in simulation length (L_x) to analyze the dissociation process particularly from different perspectives. Simulation results of the ramping simulations at heating rates of 4.0 TK/s, 0.8 TK/s and 0.4 TK/s were used for comparisons of the three properties. The definition and principles of these three physical properties will be addressed below.

3.3.1 Potential Energy

The potential energy of the system was analyzed to be able to determine the dissociation temperature regime. The principle lies in the change of internal energy during phase transition. The internal energy of the system is associated with the energy behind the random movement of particle and molecules, and it is defined as the sum of the potential and the kinetic energy of the system at constant pressure. During a phase change, the temperature of the system, which is

defined as the average kinetic energy of all particles of the system, remains statistically constant and only a change in the potential energy is observed.

With this principle, the approximate dissociation temperature can be obtained in a potential energy-temperature plot, shown in figure 13, which is the temperature region where the temperature is slowly increasing while the potential energy increases more dramatically. Since the clear change in potential energy occurs over a range of temperatures, further analysis is required by other data analysis methods, such as curve fitting or other approximation methods [63] to identify dissociation temperature. The dissociation temperature identified in this work was obtained by fitting a spline curve and calculating the inflection point of the curve with its second derivative using MATLAB [64] but it is clear that the temperature band over which the potential energy changes is quite narrow (less than 10 K). Figure 13 shows a dissociation temperature very close to 375 K, for example.

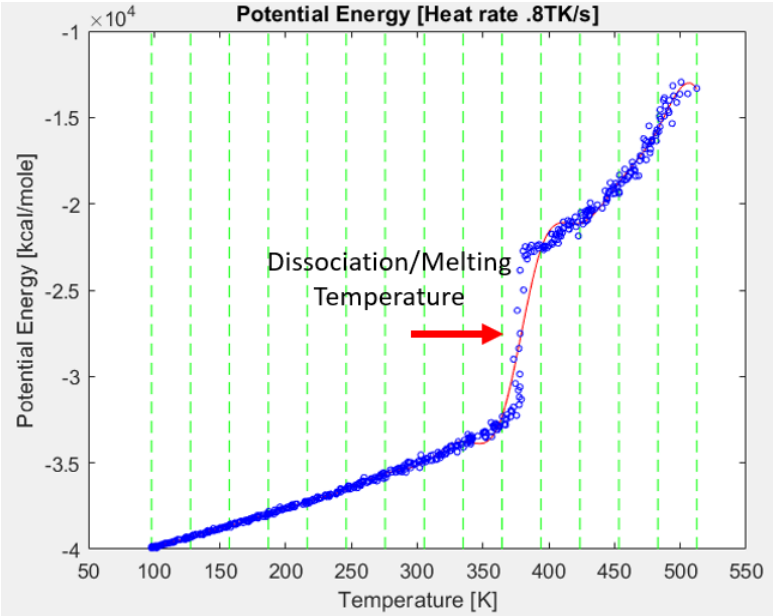

Figure 13. Potential Energy-Temperature plot at a heating rate of 0.8 TK/s, showing spline approximation.

3.3.2 Mean Squared Displacement

The mean squared displacement (MSD) is defined as the measure of position deviation of a particle with respect to a reference position over time, and it is related to the range of random movement of particles. It is described in the following equation:

$$\mathrm{MSD} \equiv \langle |\mathbf{x}(t) - \mathbf{x_0}|^2 \rangle = \frac{1}{N} \sum_{i=1}^{N} |\mathbf{x^{(i)}}(t) - \mathbf{x^{(i)}}(0)|^2$$

Where N is the number of particles to be averaged, vector $\mathbf{x^{(i)}}(0) = \mathbf{x_0^{(i)}}$ is the reference position of the i-th particle, and vector $\mathbf{x^{(i)}}(t)$ is the position of the i-th particle at time t [27-29].

The mean squared displacement is used to analyze the diffusive behavior of individual particles and it can be related to the diffusion coefficient using Einstein's diffusion equation. The Einstein diffusion equation is related to the derivative of the averaged mean squared displacement of particles as:

$$D = \frac{1}{6} \lim_{t \to \infty} \frac{\mathrm{d}}{\mathrm{d}t} \frac{1}{N} \sum_{i=1}^{N} \langle |\mathbf{r}_i(t) - \mathbf{r}_i(0)|^2 \rangle,$$

Where D is the diffusion coefficient and N is the number of particles.

This relation will then determine the diffusion coefficient by calculating the slope of the MSD-Time plot and dividing by 6. This is because, the mean squared displacement becomes a linear function of the time in the long-time limit [27-29].

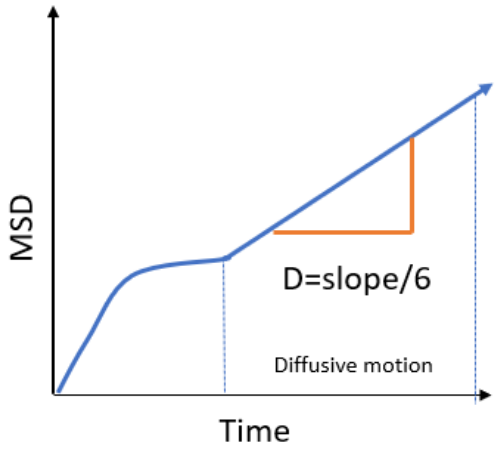

Figure 14. Mean Squared Displacement vs Time plot showing linear behavior at later times according to Einstein's Relation.

This research is focused on determining the dissociation temperature of methane hydrates, and one of the approaches is to analyze the mean squared displacement of oxygen. This is because when the dissociation occurs, water molecules, which can be represented by the oxygen atoms for simplicity, breaks out of the cage and thus increases the water molecules diffusive behavior. A dramatic increase in the MSD values can then be observed. The dissociation temperature using this analysis approach was calculated using the same method as the potential energy by fitting a spline curve and calculating the inflection point with its second derivative using MATLAB. Figure 15 demonstrates the results of MSD changing over the increased temperature with a spline shape. This method gives a dissociation temperature near 380 K, with little variation, for the conditions shown in figure 15.

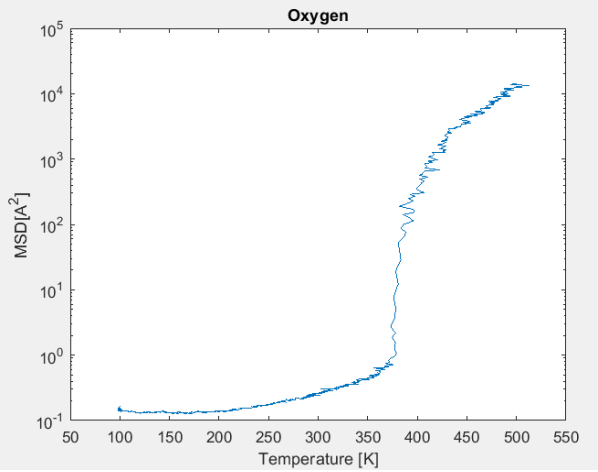

Figure 15. MSD-Temperature Plot at Heating Rate of 0.8 TK/s.

3.3.3 Simulation Box Length

Before a hydrate dissociates, the volume is constant. When the dissociation process initiates, water molecules melt and methane gas escapes which leading to a dramatic increase of the volume. This principle can therefore be used to calculate methane hydrate dissociation by analyzing the changes in simulation box length throughout the simulation.

For this purpose, this study selected a small population of the cell lengths (Figure 16) near the dissociation process by averaging over a low variability (COV<~ 1.3%) using MATLAB. The temperature at which the cell length just begins to increase is identified as the dissociation temperature for this approach.

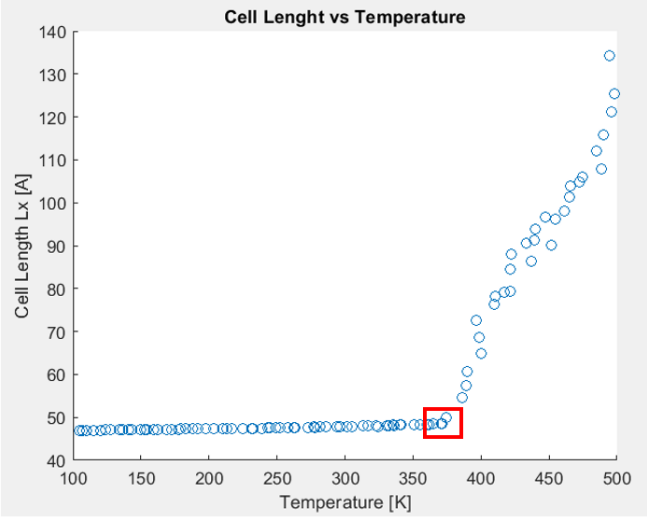

*F*igure 16. Cell Length-Temperature plot at a heating rate of 0.4 TK/s. The analyzed data points are enclosed in the red square.

3.3.4 Radial Distribution Function

The radial distribution function (RDF) defines the probability of finding a particle at a distance, r, from another tagged particle and it is described as in the following equation:

$$g(r) = \frac{dn_r}{4\pi dr * \rho}$$

Where dn_r is a function that computes the number of particles within a shell of thickness dr and density ρ [65]. The radial distribution function can be described as a histogram of the number of particles at a certain distance at a certain time, which allows observing the change in the aggregate position of particles at different times during a simulation.

In figure 17, (which comes from reference [65]) demonstrates the approach with argon by showing that the solid phase and the liquid phase argon have different behavior for the radial distribution functions. The solid argon having clear peaks that indicates the position of the cluster of atoms. There are smoother peaks for liquid argon since atoms are more evenly distributed.

Similarly, this study includes solid and liquid phase of hydrates and monitors the radial distribution function of the oxygen-oxygen interactions during the dissociation to provide a clear change in the structure as cages break and atoms are distributed along the simulation box.

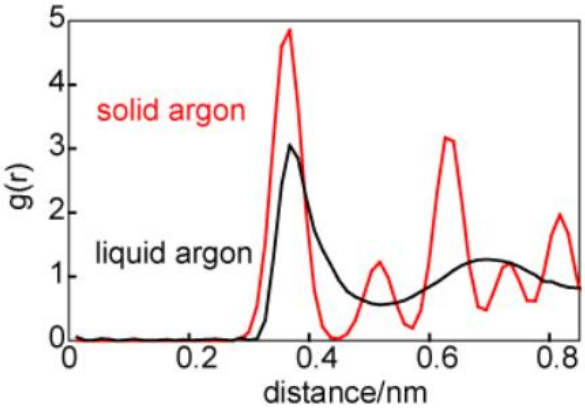

Figure 17. Radial distribution function (RDF) for Argon-Argon interactions [65].

CHAPTER 4: RESULTS AND DISCUSSION

This chapter will discuss calculation of the dissociation temperature of methane hydrate using the inflection point of the change in potential energy, mean squared displacement and cell length for temperature ramping simulations. The results were analyzed to determine the parameter that represents the dissociation temperature the best for these simulations. Furthermore, the analysis and discussion of methane hydrate as it undergoes a temperature gradually rising at a fixed rate, and how the molecules behave and interact with each other, is presented. Further, methane hydrate is simulated for a substantial step change of temperature. These results will be analyzed and compared for possible explanation of what is happening locally during hydrate dissociation, and ultimately will be used to provide insight into an optimized molecular dynamics strategy for a reasonable computational CPU effort.

4.1 Approaching Dissociation with Three Measures

As was described in the prior chapter, the determination of dissociation temperature depends on the method used to define that temperature. Hence, rather than presenting the results as an accurate calculated dissociation temperature, the differences are demonstrated as comparative measures. Table 8 shows a comparison of the dissociation temperature obtained using potential energy, mean squared displacement, and simulation box length as the three criteria for the representative heating rates 4 TK/s, 0.8 TK/s and 0.4 TK/s.

Heating Rate [TK/s]	Potential Energy	MSD	Length
4	409.6 K	394.1K	391.0K
0.8	379.1 K	367.9 K	376.6K
0.4	*371.4 K*	*354.4K*	*365.4 K*

Table 8. Dissociation temperature [K] calculated using potential energy, mean squared displacement (MSD) and cell length.

The highest dissociation temperature for all three heating rates were obtained from the potential energy definition. The results obtained from MSD and the length of the simulation box were not consistently higher or lower, that is there is not a measurable criterion computed as an overall higher or lower temperature for the three heating rates. A higher dissociation temperature was obtained at a heating rate of 4 TK/s using MSD as compared with the box length method, while it was lower for the other two heating rates. The calculation of the dissociation temperature using potential energy appears to be higher than the other 2 measures. This appears to result because the system is extremely small, and the heating rate is relatively fast for the system to adjust its energy. Note that the largest discrepancy between dissociation temperature from the 3 methods occurs at the highest heating rate. This is consistent with the expectation that the system needs an equilibration time to formally define a system temperature that can then be identified as occurring at dissociation. In particular, the distance-based measures (box length and MSD) must certainly require enough time to allow the atoms to move a noticeable distance even if their lattice bonds have been released.

After taking into account the definitions of the properties and parameters analyzed, as well as the results obtained for the calculated dissociation temperatures, using the potential energy of the system predicts higher dissociation temperature with its detailed considerations of more physical thermodynamic aspects, particularly the energy measures. This work simulates a small number of molecules rather than a large ensemble, and so the statistical measure of temperature can be skewed to a higher value. For the same reason, MSD and the box length may predict lower dissociation temperature. This research continues with using potential energy to determine dissociation temperature for the results analysis in the following sections because that measure is the most distinctive and least dependent on curve fitting. The potential energy takes into account the pair and bonding energy as well as angle, dihedral, improper long-range and fixed energy (as stated in the LAAMPS manual) and thus dissociation temperature (including the change in both MSD and box length) can be seen as an effect caused by the change in the potential energy of the atom or the whole system. Dissociation is also reflected fundamentally in the discontinuous jump in potential energy during phase change (moving from one state of matter to another).

4.2 Temperature Ramping

For temperature ramping simulations the effect of increasing temperature at different heating rates was analyzed. The dissociation temperatures at these rates were calculated. The diffusive behavior of methane molecules in large and small cages as well as oxygen atoms, which represents water molecules, were quantified with the mean squared displacement (MSD). Changes in the hydrate structure were recorded with the radial distribution function of oxygen interactions. Finally, methane molecule trajectories of displacement during dissociation were analyzed.

4.2.1 Dissociation temperature at different heating rates

We are interested in the response of the system in temperature increase at different heating rates. Therefore, we analyze the difference in dissociation temperature.

The results shown in Table 9 show that the system dissociated at a higher temperature with a higher heating rate. Figure 18 shows the dissociation temperature calculation results at different heating rates with an empirical computational error of $\pm$ 5 K for all cases as the variability of the simulations. As the temperature increases faster at higher heating rates hydrate molecules have less response time for the same temperature increase. In other words, the hydrate molecules respond to a higher temperature increase per unit time, and because of this, the dissociation occurs at a higher temperature than if the molecules were given more time to adjust at a given temperature.

Heat Rate [TK/s]	Dissociation Temperature [K]
0.4	371.5
0.8	379.2
1.0	387.6
1.3	393.7
2.0	384.3
4.0	409.6
40.0	436.9

Table 9. Dissociation temperature of the methane hydrate system at different heating rates.

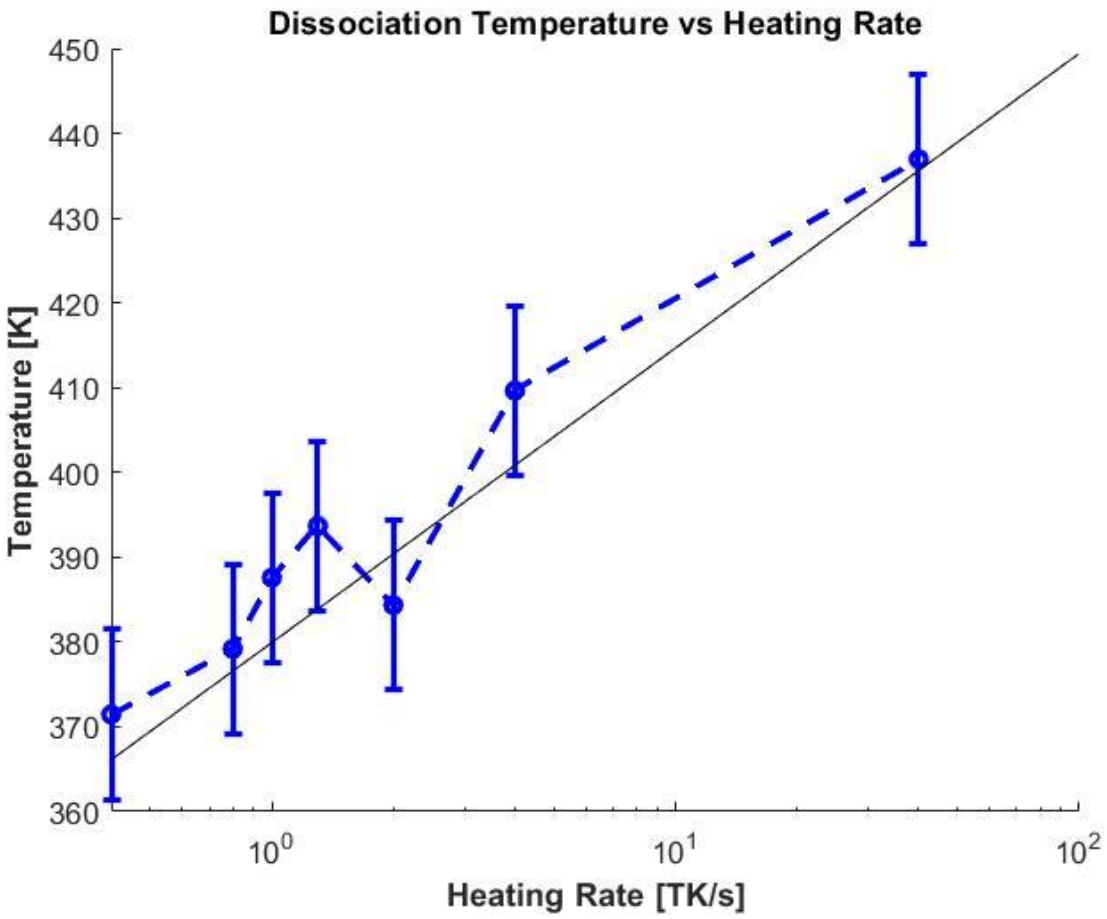

Figure 18. Dissociation temperature for methane hydrate at different heating rates with their respective 10 K error bar.

4.2.2 Mean Squared Displacement of Oxygen and Methane

During the dissociation process, the stability of molecules in hydrate cages throughout the simulation is analyzed using mean squared displacements of oxygen atoms, representing water molecules, and methane in large and small cages. In order to observe a clear difference of the MSD results, there are two heating rates selected from the seven. One is a relatively low heating rate at 0.4 TK/s, and the other is a high heating rate at 4 TK/s.

The result is shown in figure 19. Beside the distinct difference in dissociation temperature for the system described above, oxygen atoms exhibit correspondent mean squared displacement value to

methane for a heating rate at 4 TK/s. This indicates a similar diffusive behavior for methane and water, particularly at a high heating rate. While at a lower heating rate the mean squared displacement of methane in both large and small cages is clearly higher than that of oxygen, which indicates a higher diffusive behavior with respect to water.

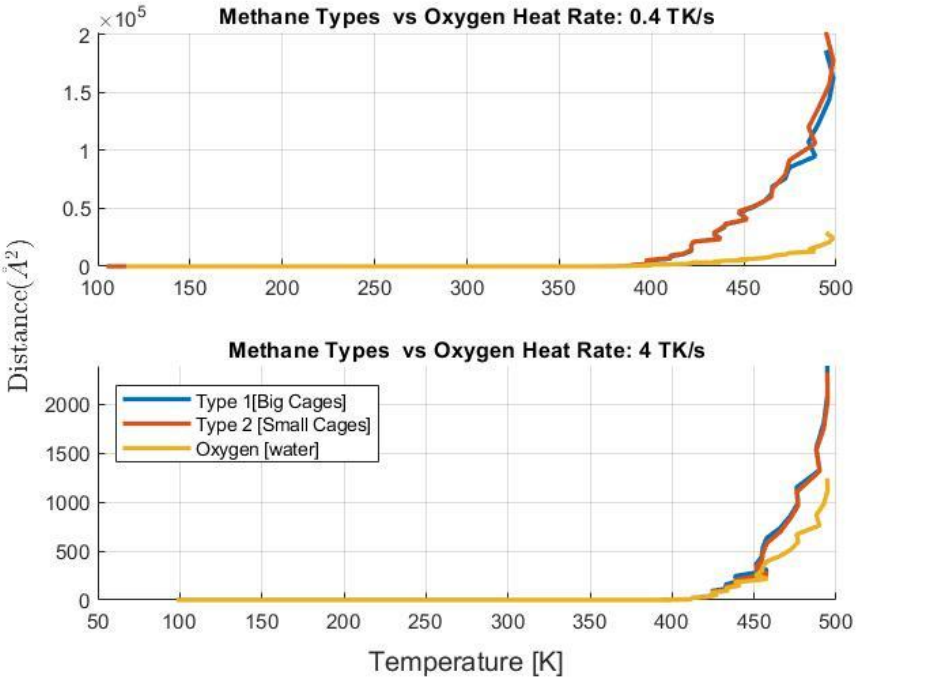

Figure 19. Mean squared displacement of oxygen atoms representing water molecules, in yellow. Methane molecules in large cages and small cages in blue and red respectively. Two heating rates, 0.4 TK/s (top) and 4 TK/s (bottom) are shown.

4.2.3 Radial Distribution Functions of Oxygen-Oxygen Interactions

The RDF information of the evolution in the methane hydrate structure during dissociation is plotted in figure 20. The RDF of oxygen-oxygen interaction representing the water molecules and the hydrate cages formed by them, which has a cutoff distance of 12 Å, the length of the unit cell, at 5 different stages of dissociation determined by potential energy plots and trajectory files, were extracted. To study the influence of the heating rate, as in the MSD study, the results for the RDFs for a heating rate of 0.4 TK/s and 4 TKs were analyzed. The results in figure 20 clearly show

characteristics of a solid methane hydrate at an early time of dissociation (ex: 670 ps), with clear valleys representing an ordered methane hydrate crystalline structure. The structure gradually disappears at later times until the RDF curve flattens as is characteristic of liquid water. The comparison of heating rate shows that more time is needed for a methane hydrate to dissociate at a heating rate of 0.4TK/s as compared to a duration of 5 ps at a high heating rate of 4 TK/s, which represents a low heating rate with a duration of 30 ps.

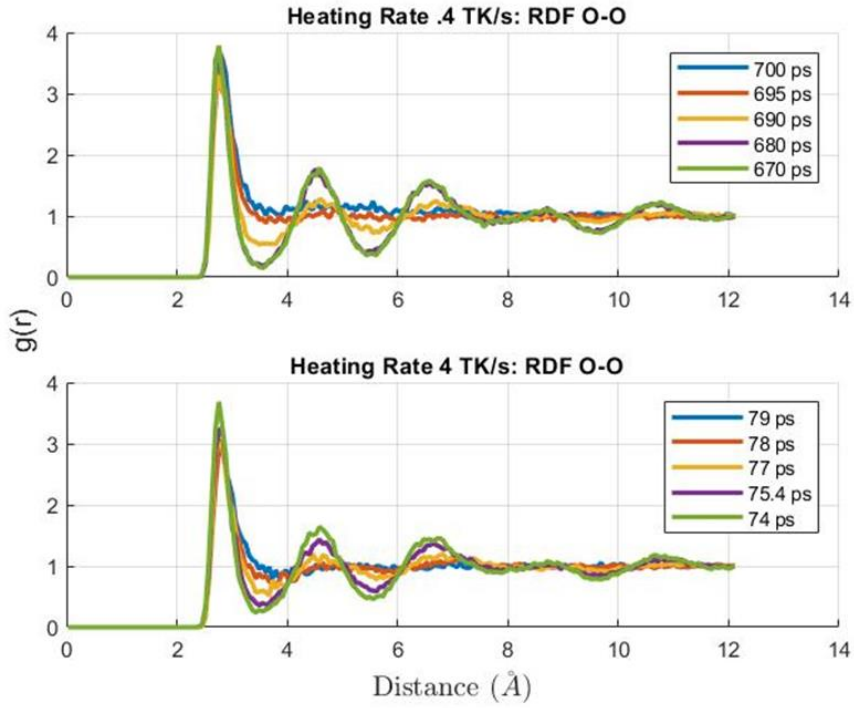

Figure 20. Radial Distribution Function of oxygen- oxygen interaction representation the at 5 different time stages of dissociation for a heating rate of 0.4 TK/s and 4 TK/s.

4.2.4 Discussion

The methane hydrate dissociation behavior shows that the dissociation temperature increases with an increasing heating rate, as temperature increases more rapidly, and the system responds tardily. Mean squared displacement results of the dissociation temperature, (MSD) and (RDF), demonstrate that the homogeneity of the dissociation process is independent of heating rate, because values for MSD of methane molecules located in large cages and small cages do not

exhibit a significant difference. This is consistent with the visual images of the displacement trajectories at three different dissociation times 670, 690, and 700 ps, in figure 21. The displacement trajectory of methane at heating rate 0.4 TK/s in large (top red) and small cages (bottom pink) showed no distinct preference for escaping either cage first for all of the three dissociation times. An enlarged portion of the hydrate structure is shown in the middle row to facilitate visualization of structure evolution during dissociation. The same behavior was observed by Gupta in 2007 [66]. In that work, NMR was performed for methane hydrate during dissociation, and both cages showed similar decomposition rates with no clear preference.

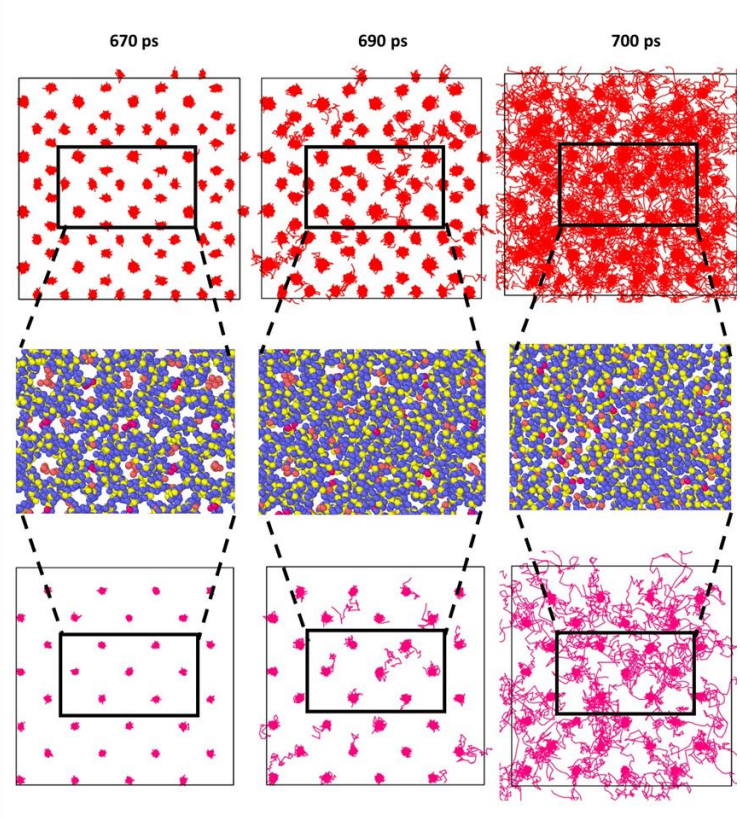

Figure 21. Methane molecules displacement located at large cages (Top) and small cages (Bottom) and as enlarged portion of the hydrate structure (Middle) are showed at a heating rate of 0.4 TK/s at different times of dissociation in picoseconds.

Comparing the mean squared displacement at a high and low heating rate, a clear difference in behavior of water molecules is observed. While at low heating rate, the MSD values of oxygen and methane show great difference, that difference is reduced significantly at high heating rate. This could be an indicator of evaporation with similar diffusive behavior between water molecules and methane gas.

The radial distribution function at high and low heating rates showed the same structure changes during the dissociation at both high and low heating rates. However, the process occurs faster at a higher heating rate.

4.3 Temperature Step

For temperature step simulations, the effect of constant step increments of temperature for observing the dissociation process were conducted. The dissociation initiation time at each temperature step was calculated. Similarly, to the previous section (temperature ramping) the result of mean squared displacement (MSD) and (RDF) during the dissociation period are presented.

4.3.1 Dissociation Starting Time At Different Temperature Steps

The dissociation time is shown in Table 10, which represents the time for the system to start dissociating using both the potential energy and trajectory movements to determine the dissociation initiation. The details of this analysis process are described in Section 3.3. The results show that the system starts to dissociate sooner at a larger ΔT while the system does not dissociate at a ΔT of 80 K which was the limit of the simulations.

Final Temperature [K]	Dissociation Start Time [ps]	Temperature Step Size [K]
350	NO DISS	80
355	265.4	85
360	277.0	90
365	127.4	95
370	57.9	100

Table 10. The time of the hydrate started to dissociate at different temperature steps.

4.3.2 Mean Squared Displacement

The plots of the mean squared displacement for oxygen and methane in small and large cages during temperature step simulations are shown in figure 22. The results are very similar for all the 3 selected temperatures, showing a clear difference for oxygen, representing water in solid and later in liquid state, and methane. The methane gas showed more diffusive activity than water.

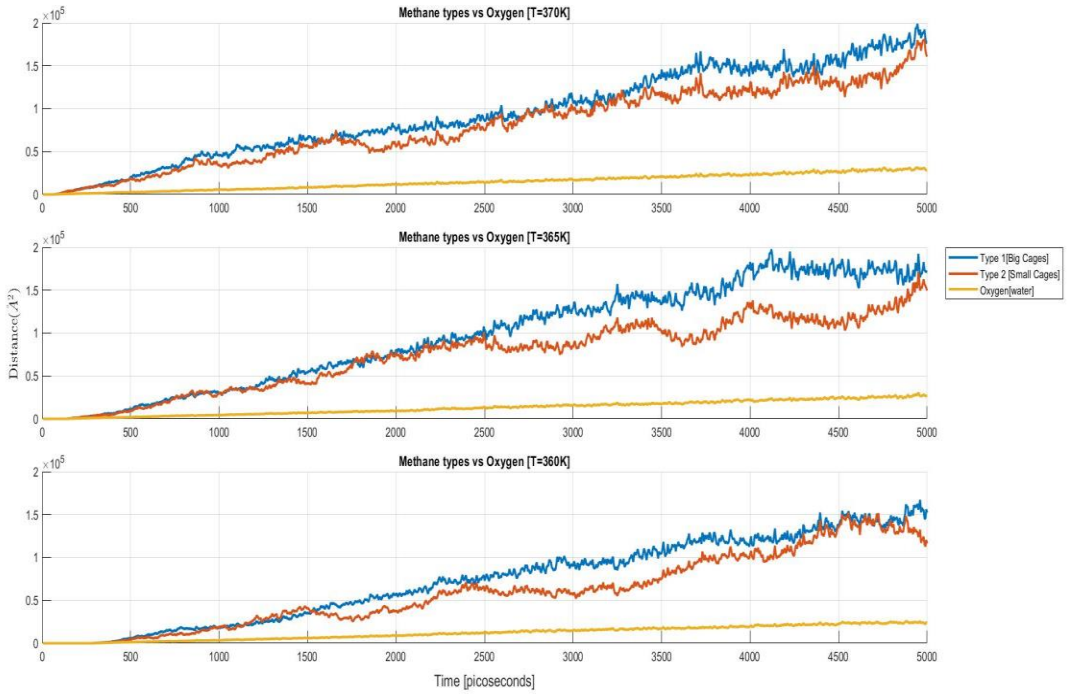

Figure 22. Mean squared displacement of Oxygen atoms representing water molecules, in yellow and methane molecules in large cages and small cages in blue and red respectively, at a 370 K, (Top), 365 K (Middle) and 360 K (Bottom).

4.3.3 Diffusion Coefficient

The diffusion coefficients were calculated at constant temperature during the simulated 5ns for oxygen, methane in small and large cages as shown in Table 11. While oxygen diffusion coefficient is clearly lower than the methane diffusion coefficient hosted in both cages, the difference of the diffusion coefficient doesn't change significantly independently of the size of the cage occupied. The results are consistent with the mean squared displacement analysis.

	H_2O $[cm^2/s]$	CH_4 $[cm^2/s]$	
T [K]	Oxygen	TYPE 1	TYPE 2
370	1.01E-04	5.88E-04	5.0133-04
365	9.22E-05	6.77E-04	4.62E-04
360	8.89E-05	5.51E-04	4.79E-04

Table 11. Diffusion coefficient of oxygen, methane type 1, located in large cages, and methane type 2, located in small cages.

4.3.4 Radial Distribution Function of Oxygen- Oxygen Interactions

Like the previous temperature ramping simulations, the radial distribution functions at 5 different time stages of dissociation were plotted to observe the changes in the structure. The RDFs at 370 K, 365 K and 360 K are shown in figure 23, and all the 3 plots show a gradual dissociation of the hydrate structure. There is an important aspect to note that the duration of the dissociation process, at 370 K was 20 ps, at 360 K dissociation lasted 30 ps, and at 365 K the dissociation was faster at 12 ps. These dissociation time results based on RDF are approximate time data since the values are limited by the time interval between frames of the trajectory files.

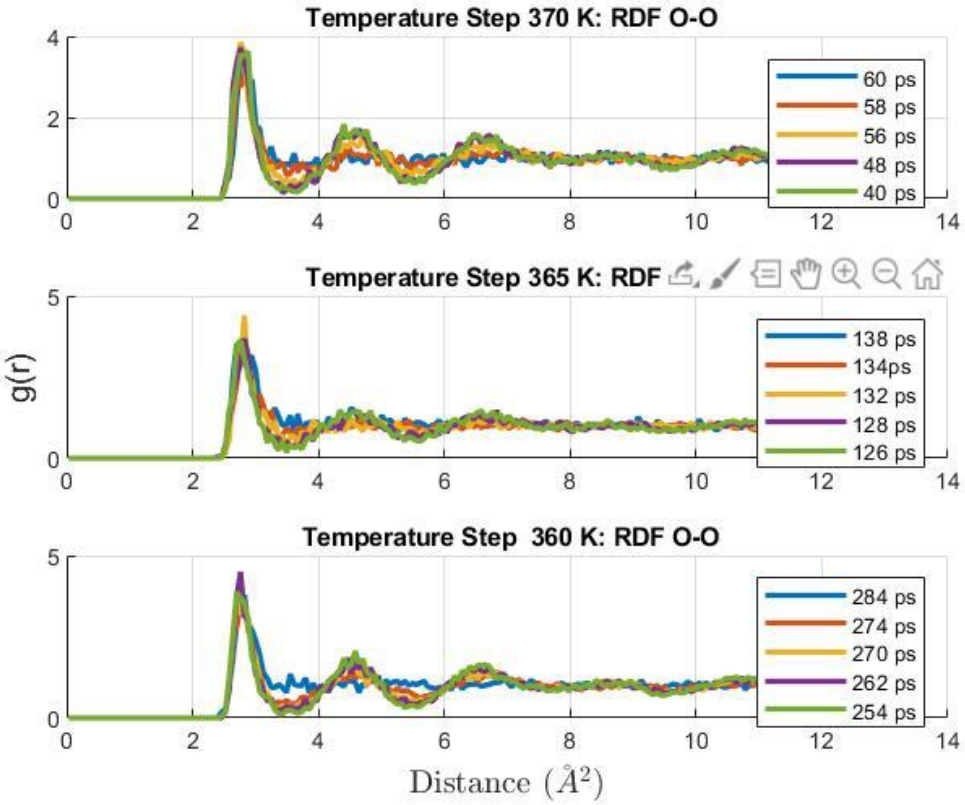

Figure 23. Radial distribution function of Oxygen-Oxygen Interactions, representing. water molecules structure for a temperature step of 370 K (Top), 365 K (Middle) and 360 K (Bottom) at five different time stages of dissociation.

4.3.5 Discussion

The methane hydrate simulation at 5 temperature steps, 370 K, 365 K, 360 K, 355 K and 350 K showed that dissociation was not achieved at 350 K, which is at the smaller temperature step of 80 K from 270 K, while the dissociation occurred faster and sooner at a larger temperature step. The mean squared displacement at different temperature steps showed similar diffusive behavior of all the molecules. There was not a clear difference between methane in small and large cages and oxygen (which represents water). Overall, water has less diffusive activity than methane gas. These results are consistent with the diffusion coefficient values for oxygen and methane. The difference in MSD values for methane contained in small and large cages show random behavior after the

offset point (dissociation temperature), which is close to the ending time of dissociation calculated with the potential energy and structure change.

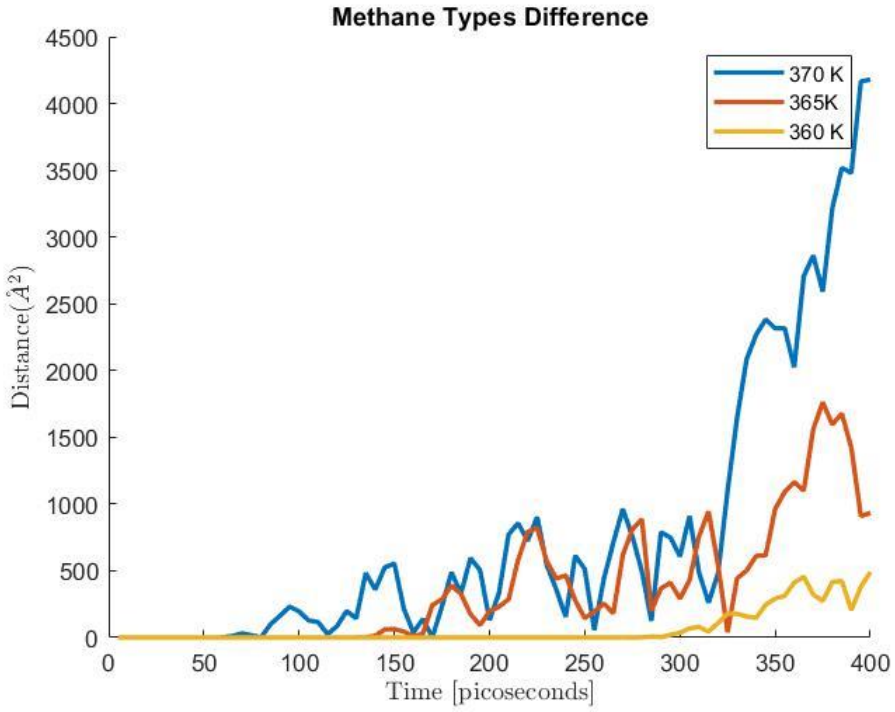

Figure 24. Mean square displacement difference between methane molecules in small and large cages at temperature steps of 370, 365 and 360 K.

The radial distribution function results showed the evolution of the methane hydrate structure during dissociation at different temperature steps, and it proved that even if the process lasts differently as steps increment, the hydrate will follow a very similar procedure for dissociation.

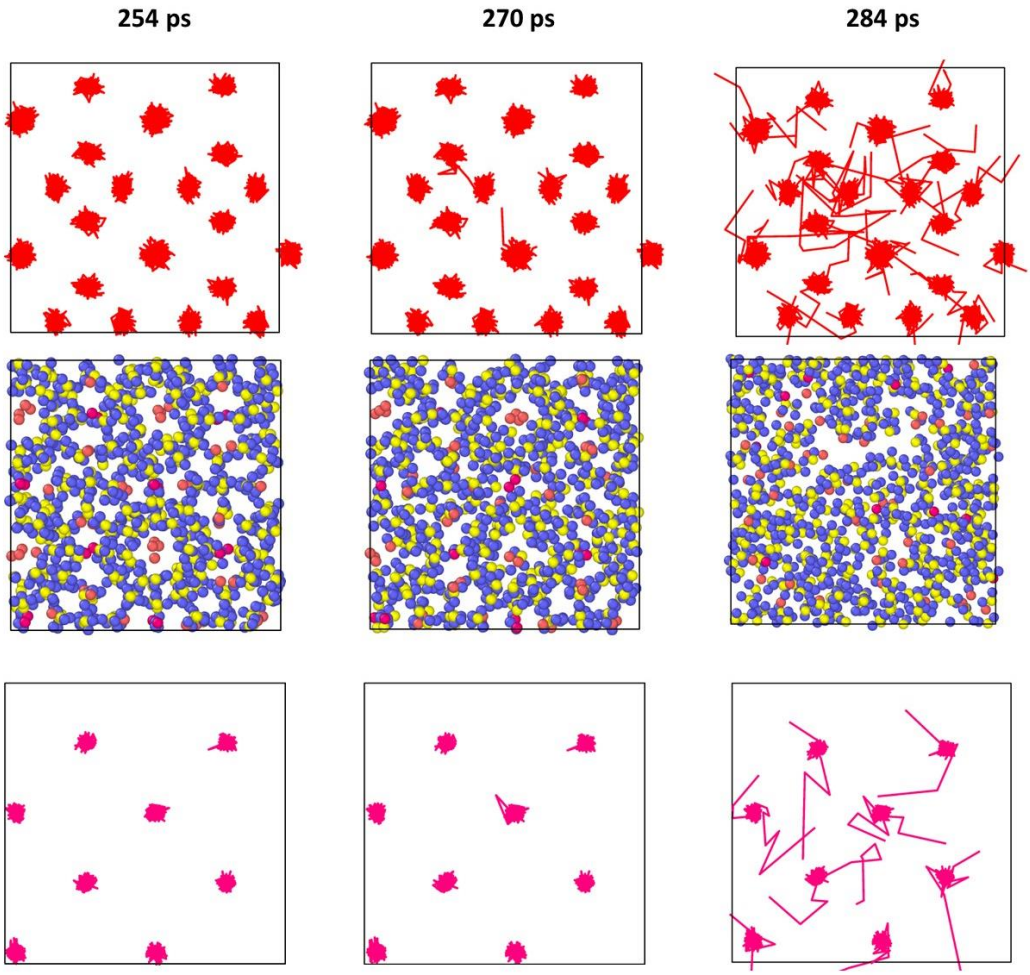

Figure 25. Methane molecules displacement located at large cages (Top) and small cages (Bottom) at a heating rate of 0.4 TK/s at different times of dissociation in picoseconds.

CHAPTER 5: CONSLUSIONS AND FUTURE OF MOLECULAR DYNAMICS SIMULATION FOR METHANE HYDRATES

This work simulates temperature step and ramping for methane hydrate to induce dissociation. Methane molecules in large and small cages were classified and analyzed to learn if there was a difference in the large or small cages for dissociation. Both types of simulations showed a homogeneous dissociation, meaning there was not a significant difference in the time of dissociation between small and large cages. This was determined by the diffusion coefficient in step simulations and the difference in mean squared displacement in ramping simulations.

In temperature step simulations, dissociation occurred earlier and in less time at a larger ΔT while cases with a temperature step under 355K were not able to dissociate during the simulated 5ns. The difference between the mean squared displacement of methane molecules in small and large cages increased significantly at the end of the dissociation time. The behavior of the mean squared displacement after dissociation, which was calculated with potential energy and radial distribution functions, can be described as random. The diffusion coefficient for methane molecules in large cages was slightly higher than for the methane molecules trapped in small cages.

Ramping simulations showed a relatively large uncertainty for dissociation temperature calculations, this can be caused from the fast increase in temperature without letting the system equilibrate; slower heating rates showed a more defined potential energy and mean square displacement curve which are better for the calculation of thermodynamical properties.

To conclude, for the MD simulation of this work, temperature step simulations are better for analyzing the relationship between physical and thermodynamical properties. While slow heating

rates of the temperature ramping show a slower structure change which can allow the analysis of specific cage dissociation more thoroughly.

The effects of pressure, temperature and cage occupancy for methane have been widely studied at different scales, including molecular dynamics scale as in this work. Moreover, most molecular dynamics studies were accomplished by simulating a sole methane hydrate system, meaning merely one hydrate cell and with only a single guest molecule type.

Methane hydrates are naturally found in outer continental areas where they are exposed to liquid water and seafloor sediments so that the environment can change the hydrate stability conditions. To be able to develop efficient methane gas extraction methods, these factors must be considered for simulating a realistic scenario. There are several works that have made efforts for modeling realistic conditions of methane hydrates in recent years. Fang et al 2019 [67] studied the heat induced dissociation in a system consisting of a methane hydrate phase which is sandwiched by a sandy nanopore phase and a bulk phase outside of the pore, providing a realistic representation of methane hydrates in nature. It would be valuable to have more of this kind of simulation accomplished.

As mentioned previously in [3] large scale methane extraction from hydrates have been achieved, but not yet with the performance needed for practical vast production and even gas storage. There are three phases involved during the extraction process in the hydrate systems. They are gas phase for the guest molecules, liquid water phase, and solid water phase, and this 3-phase problem has gained interest [68]. Consequently, in order to achieve sustainable and low-carbon processes, molecular simulations of multiphase systems for studying CO_2 -CH_4 guest molecule exchange in hydrate need also be performed. The ultimate purpose of such study is to sequester CO_2 in the deep

ocean, and researchers have been taking different approaches to this problem such as the settings of the initial configuration, surrounding methane hydrate with liquid CO_2 [69] .

As technology advances and computational capabilities expand, it is possible to perform molecular simulation for a more complex system. This gives the opportunity to optimize and understand the more complicated interactions of the molecular dynamics system discussed above, ex: CO_2 -CH_4 exchanging process.

Experimental efforts in optimizing methane extraction or inhibiting hydrate formation in pipelines using surfactants have been researched [70, 71] but more work in this field is needed . Moreover the molecular dynamics simulation development in recent years is to explore and be able to model large inhibitor molecules and, surfactants [72, 73]. Therefore, and to conclude, the molecular studies of small and large molecules of surfactants in multiphase systems are yet to be thoroughly studied. This will be the future direction of the current thesis work.

Bibliography

[1] T. Collett, A. Johnson, C. Knapp, and R. Boswell, *Natural Gas Hydrates—Energy Resource Potential and Associated Geologic Hazards*. 2020. doi: 10.1306/m891320.

[2] M. E. Holland, P. J. Schultheiss, and J. A. Roberts, "Gas hydrate saturation and morphology from analysis of pressure cores acquired in the Bay of Bengal during expedition NGHP-02, offshore India," *Mar. Pet. Geol.*, vol. 108, no. April 2018, pp. 407–423, 2019, doi: 10.1016/j.marpetgeo.2018.07.018.

[3] T. S. Collett, W. F. Agena, M. W. Lee, M. V Zyrianova, K. J. Bird, T. C. Charpentier, D. W. Houseknect, T. R. Klett, R. M. Pollastro, and C. J. Schenk, "Assessment of gas hydrate resources on the North Slope, Alaska, 2008.," *U.S. Geol. Surv.*, 2008.

[4] S. R. (eds) Beaudoin, Y. C., Waite, W., Boswell, R. and Dallimore, "Frozen Heat: A UNEP Global Outlook on Methane Gas Hydrates.," *United Nations Environ. Program. GRID-Arendal.*, vol. 1, 2014.

[5] A. Johnson, "Global resource potential of gas hydrate–A new calculation," *Nat. Gas Oil*, 2011.

[6] M. Frye, "Preliminary evaluation of in-place gas hydrate resources: Gulf of Mexico Outer Continental Shelf," OCS Report MMS, U.S. Department of the Interior Minerals Management Service Resource Evaluation Division, Washington D.C, 2008.

[7] T. Fujii, T. Saeki, T. Kobayashi, T. Inamori, M. Hayashi, O. Takano, T. Takayama, T. Kawasaki, S. Nagakubo, M. Nakamizu, and K. Yokoi, "Resource Assessment of Methane Hydrate in the Eastern Nankai Trough, Japan," 2008. doi: 10.4043/19310-ms.

[8] G. J. Crutchley, G. Maslen, I. A. Pecher, and J. J. Mountjoy, "High-resolution seismic velocity analysis as a tool for exploring gas hydrate systems: An example from New Zealand's southern Hikurangi margin," *Interpretation*, 2016, doi: 10.1190/INT-2015-0042.1.

[9] B. J. Ryu, T. S. Collett, M. Riedel, G. Y. Kim, J. H. Chun, J. J. Bahk, J. Y. Lee, J. H. Kim, and D. G. Yoo, "Scientific results of the Second Gas Hydrate Drilling Expedition in the Ulleung Basin (UBGH2)," *Mar. Pet. Geol.*, 2013, doi: 10.1016/j.marpetgeo.2013.07.007.

[10] T. S. Collett, R. Boswell, W. F. Waite, P. Kumar, S. K. Roy, K. Chopra, S. K. Singh, Y. Yamada, N. Tenma, J. Pohlman, and M. Zyrianova, "India National Gas Hydrate Program Expedition 02 Summary of Scientific Results: Gas hydrate systems along the eastern continental margin of India," *Mar. Pet. Geol.*, 2019, doi: 10.1016/j.marpetgeo.2019.05.023.

[11] J. Wang, S. Wu, X. Kong, Q. Li, J. Wang, and R. Ding, "Geophysical characterization of a fine-grained gas hydrate reservoir in the Shenhu area, northern South China Sea: Integration of seismic data and downhole logs," *Mar. Pet. Geol.*, 2018, doi: 10.1016/j.marpetgeo.2018.03.020.

[12] "Assessment of Gas Hydrate Resources of the U.S. Lower-48 Outer Continental Shelf.," 2012.

[13] "Methane Hydrates," *World Ocean Review*, 2020. https://worldoceanreview.com/en/wor-3/methane-hydrate/extraction/

[14] E. D. Sloan, "Clathrate Hydrates of Natural Gas." p. 641 pp., 2008.

[15] H. Hirai, T. Kondo, M. Hasegawa, T. Yagi, Y. Yamamoto, T. Komai, K. Nagashima, M. Sakashita, H. Fujihisa, and K. Aoki, "Methane Hydrate Behavior under High Pressure," *J. Phys. Chem. B*, 2000, doi: 10.1021/jp9926490.

[16] H. Hirai, Y. Uchihara, H. Fujihisa, M. Sakashita, E. Katoh, K. Aoki, K. Nagashima, Y. Yamamoto, and T. Yagi, "High-pressure structures of methane hydrate observed up to 8 GPa at room temperature," *J. Chem. Phys.*, 2001, doi: 10.1063/1.1403690.

[17] I. M. Chou, A. Sharma, R. C. Burruss, J. Shu, H. K. Mao, R. J. Hemley, A. F. Goncharov, L. A. Stern, and S. H. Kirby, "Transformations in methane hydrates," *Proc. Natl. Acad. Sci. U. S. A.*, 2000, doi: 10.1073/pnas.250466497.

[18] Q. Sun, T. Y. Duan, H. F. Zheng, J. Q. Ji, and X. Y. Wu, "Phase transformation of methane hydrate under high pressure," *J. Chem. Phys.*, 2005, doi: 10.1063/1.1830411.

[19] E. D. Sloan and F. Fleyfel, "A molecular mechanism for gas hydrate nucleation from ice," *AIChE J.*, 1991, doi: 10.1002/aic.690370902.

[20] B. Muller-Bongartz, T. R. Wildeman, and E. D. Sloan, "Hypothesis for hydrate nucleation phonemena," 1992.

[21] R. Radhakrishnan and B. L. Trout, "A new approach for studying nucleation phenomena using molecular simulations: Application to CO2 hydrate clathrates," *J. Chem. Phys.*, 2002, doi: 10.1063/1.1485962.

[22] Long. J, "Gas Hydrate Formation Mechanism and Its Kinetic Inhibition," Colorado School of Mines, 1994.

[23] B. Kvamme, "A unified nucleation theory for the kinetics of hydrate formation," 2000. doi: 10.1111/j.1749-6632.2000.tb06804.x.

[24] H. Hong, M. Pooladi-Darvish, and P. R. Bishnoi, "Analytical modelling of gas production from hydrates in porous media," *J. Can. Pet. Technol.*, 2003, doi: 10.2118/03-11-05.

[25] L. A. Stern, S. Circone, S. H. Kirby, and W. B. Durham, "Temperature, pressure, and compositional effects on anomalous or 'self' preservation of gas hydrates," *Can. J. Phys.*, 2003, doi: 10.1139/p03-018.

[26] L. Chen and S. Merey, "Emerging technologies in methane hydrate projects," in *Oceanic Methane Hydrates*, 2021. doi: 10.1016/b978-0-12-818565-0.00012-4.

[27] D. Frenkel and B. Smit, *Understanding molecular simulation: From algorithms to applications*. 1996.

[28] S.Yip, *Handbook of Materials Modeling*. 2005.

[29] M. E. Tuckerman, *Statistical Mechanics: Theory and Molecular Simulation*, 1st Editio. Oxford University Press, 2010.

[30] Sandia National Laboratories, "LAAMPS Documentation," *Sandia National Laboratories*, 2020. https://lammps.sandia.gov/doc/Manual.html

[31] A. C. Paul Flowers, Klaus Theopold, Richard Langley, Paul Peter Urone, Roger Hinrichs, Manjula Sharma, Kim Dirks, "Coulomb's Law and the Electrostatic Potential," 2019. https://chem.libretexts.org/@go/page/119817

[32] S. B. Sinnott and D. W. Brenner, "Three decades of many-body potentials in materials research," *MRS Bull.*, vol. 37, no. 5, pp. 469–473, 2012, doi: 10.1557/mrs.2012.88.

[33] H. Heinz, T. J. Lin, R. Kishore Mishra, and F. S. Emami, "Thermodynamically consistent force fields for the assembly of inorganic, organic, and biological nanostructures: The INTERFACE force

field," *Langmuir*, vol. 29, no. 6, pp. 1754–1765, 2013, doi: 10.1021/la3038846.

[34] J. E. Lennard-Jones, "On the determination of molecular fields," *Proc. R. Soc. London*, 1924, doi: 10.1098/rspa.1924.0082.

[35] H. Heinz, R. A. Vaia, B. L. Farmer, and R. R. Naik, "Accurate simulation of surfaces and interfaces of face-centered cubic metals using 12-6 and 9-6 lennard-jones potentials," *J. Phys. Chem. C*, 2008, doi: 10.1021/jp801931d.

[36] A. Glielmo, C. Zeni, and A. De Vita, "Efficient nonparametric n -body force fields from machine learning," *Phys. Rev. B*, vol. 97, no. 18, pp. 1–12, 2018, doi: 10.1103/PhysRevB.97.184307.

[37] P. J. Hoogerbrugge and J. M. V. A. Koelman, "Simulating microscopic hydrodynamic phenomena with dissipative particle dynamics," *EPL*. 1992. doi: 10.1209/0295-5075/19/3/001.

[38] M. F. Harrach and B. Drossel, "Structure and dynamics of TIP3P, TIP4P, and TIP5P water near smooth and atomistic walls of different hydroaffinity," *J. Chem. Phys.*, 2014, doi: 10.1063/1.4872239.

[39] H. J. C. Berendsen, J. R. Grigera, and T. P. Straatsma, "The missing term in effective pair potentials," *J. Phys. Chem.*, vol. 91, no. 24, pp. 6269–6271, 1987, doi: 10.1021/j100308a038.

[40] K. Toukan and A. Rahman, "Molecular-dynamics study of atomic motions in water," *Phys. Rev. B*, vol. 31, no. 5, pp. 2643–2648, 1985, doi: 10.1103/PhysRevB.31.2643.

[41] W. L. Jorgensen, J. Chandrasekhar, J. D. Madura, R. W. Impey, and M. L. Klein, "Comparison of simple potential functions for simulating liquid water," *J. Chem. Phys.*, vol. 79, no. 2, pp. 926–935, 1983, doi: 10.1063/1.445869.

[42] R. García Fernández, J. L. F. Abascal, and C. Vega, "The melting point of ice Ih for common water models calculated from direct coexistence of the solid-liquid interface," *J. Chem. Phys.*, vol. 124, no. 14, 2006, doi: 10.1063/1.2183308.

[43] W. L. Jorgensen and J. Tirado-Rives, "Potential energy functions for atomic-level simulations of water and organic and biomolecular systems," *Proc. Natl. Acad. Sci. U. S. A.*, vol. 102, no. 19, pp. 6665–6670, 2005, doi: 10.1073/pnas.0408037102.

[44] J. L. F. Abascal and C. Vega, "A general purpose model for the condensed phases of water: TIP4P/2005," *J. Chem. Phys.*, vol. 123, no. 23, pp. 1–12, 2005, doi: 10.1063/1.2121687.

[45] B. Guillot, "A reappraisal of what we have learnt during three decades of computer simulations on water," *Acad. Manag. J.*, vol. 5, no. 3, pp. 219–260, 2002.

[46] M. G. Martin and J. I. Siepmann, "Transferable potentials for phase equilibria. 1. United-atom description of n-alkanes," *J. Phys. Chem. B*, 1998, doi: 10.1021/jp972543+.

[47] W. L. Jorgensen, J. D. Madura, and C. J. Swenson, "Optimized Intermolecular Potential Functions for Liquid Hydrocarbons," *J. Am. Chem. Soc.*, vol. 106, no. 22, pp. 6638–6646, 1984, doi: 10.1021/ja00334a030.

[48] J. I. Siepmann, S. Karaborni, and B. Smit, "Simulating the critical behaviour of complex fluids," *Nature*, vol. 365, no. 6444. pp. 330–332, 1993. doi: 10.1038/365330a0.

[49] U. . D. of Commerce, "The Thermophysical Properties of Methane, from 90 to 500K at pressure to 700 Bar.," 1974.

[50] A. S. Teja, R. J. Lee, D. Rosenthal, and M. Anselme, "Correlation of the critical properties of alkanes

and alkanols," *Fluid Phase Equilib.*, vol. 56, no. C, pp. 153–169, 1990, doi: 10.1016/0378-3812(90)85100-O.

[51] F. Ï. Gaden and U. S. A. Florida, "Thermostats in Molecular Dynamics," vol. 3, no. 1, pp. 1–4.

[52] L. Y. Ding, C. Y. Geng, Y. H. Zhao, and H. Wen, "Molecular dynamics simulation on the dissociation process of methane hydrates," *Mol. Simul.*, 2007, doi: 10.1080/08927020701528524.

[53] Y. Iwai, H. Nakamura, Y. Arai, and Y. Shimoyama, "Analysis of dissociation process for gas hydrates by molecular dynamics simulation," *Mol. Simul.*, vol. 36, no. 3, pp. 246–253, 2010, doi: 10.1080/08927020903307529.

[54] E. M. Myshakin, H. Jiang, R. P. Warzinski, and K. D. Jordan, "Molecular dynamics simulations of methane hydrate decomposition," *J. Phys. Chem. A*, vol. 113, no. 10, pp. 1913–1921, 2009, doi: 10.1021/jp807208z.

[55] J. Kondori, S. Zendehboudi, and L. James, "New insights into methane hydrate dissociation: Utilization of molecular dynamics strategy," *Fuel*, 2019, doi: 10.1016/j.fuel.2019.02.125.

[56] L. C. Jacobson and V. Molinero, "A methane-water model for coarse-grained simulations of solutions and clathrate hydrates," *J. Phys. Chem. B*, vol. 114, no. 21, pp. 7302–7311, 2010, doi: 10.1021/jp1013576.

[57] U. of I. at Urbana-Champaign, "VMD Visual Molecular Dynamics," *University of Illinois at Urbana-Champaign*, 2020. https://www.ks.uiuc.edu/Research/vmd/

[58] A. Stukowski, "Visualization and analysis of atomistic simulation data with OVITO-the Open Visualization Tool," *Model. Simul. Mater. Sci. Eng.*, vol. 18, no. 1, Jan. 2010, doi: 10.1088/0965-0393/18/1/015012.

[59] E. Z. and G. R. H. Marcus D Hanwell,DonaldECurtis, David C Lonie, Tim Vandermeersch, "Avogadro: an advanced semantic chemical editor, visualization, and analysis platform," *J. Cheminform.*, vol. 4, no. 17, 2012, doi: 10.1186/1758-2946-4-17.

[60] M. T. Kirchner, R. Boese, W. E. Billups, and L. R. Norman, "Gas hydrate single-crystal structure analyses," *J. Am. Chem. Soc.*, vol. 126, no. 30, pp. 9407–9412, 2004, doi: 10.1021/ja049247c.

[61] B. Kvamme, "Enthalpies of hydrate formation from hydrate formers dissolved in water," *Energies*, vol. 12, no. 6, 2019, doi: 10.3390/en12061039.

[62] E. M. Yezdimer, P. T. Cummings, and A. A. Chialvo, "Determination of the Gibbs free energy of gas replacement in SI clathrate hydrates by molecular simulation," *J. Phys. Chem. A*, vol. 106, no. 34, pp. 7982–7987, 2002, doi: 10.1021/jp020795r.

[63] C. J. Adkins, *Equilibrium Thermodynamics*. 1983. doi: 10.1017/cbo9781139167703.

[64] 2019 The Mathworks, Inc. MATLAB, Version 9.6, "MATLAB 2019b - MathWorks," *Www.Mathworks.Com/Products/Matlab*. 2019.

[65] U. of Oxford, "Introduction., Liquids and Solutions: 2nd Year Michaelmas Term," *University of Oxford*. http://rkt.chem.ox.ac.uk/lectures/liqsolns/liquids.html

[66] A. Gupta, S. F. Dec, C. A. Koh, and E. D. Sloan, "NMR investigation of methane hydrate dissociation," *J. Phys. Chem. C*, vol. 111, no. 5, pp. 2341–2346, 2007, doi: 10.1021/jp066536+.

[67] B. Fang, F. Ning, W. Ou, D. Wang, Z. Zhang, Y. Yu, H. Lu, J. Wu, and T. J. H. Vlugt, "The dynamic behavior of gas hydrate dissociation by heating in tight sandy reservoirs: A molecular dynamics

simulation study," *Fuel*, vol. 258, no. June, 2019, doi: 10.1016/j.fuel.2019.116106.

[68] Z. Sun, H. Wang, J. Yao, Z. Sun, K. Bongole, X. Zhu, L. Liu, and J. Wang, "Effect of cage-specific occupancy on the dissociation rate of a three-phase coexistence methane hydrate system: A molecular dynamics simulation study," *J. Nat. Gas Sci. Eng.*, 2018, doi: 10.1016/j.jngse.2018.05.004.

[69] Y. Iwai, H. Nakamura, and M. Hirata, "Molecular dynamics simulation of replacement of methane hydrate with carbon dioxide," *Mol. Simul.*, vol. 38, no. 6, pp. 481–490, 2012, doi: 10.1080/08927022.2011.647817.

[70] O. Nashed, D. Dadebayev, M. S. Khan, C. B. Bavoh, B. Lal, and A. M. Shariff, "Experimental and modelling studies on thermodynamic methane hydrate inhibition in the presence of ionic liquids," *J. Mol. Liq.*, vol. 249, pp. 886–891, 2018, doi: 10.1016/j.molliq.2017.11.115.

[71] A. Heydari and K. Peyvandi, "Role of metallic porous media and surfactant on kinetics of methane hydrate formation and capacity of gas storage," *J. Pet. Sci. Eng.*, vol. 181, no. March, p. 106235, 2019, doi: 10.1016/j.petrol.2019.106235.

[72] W. Lin, G. J. Chen, C. Y. Sun, X. Q. Guo, Z. K. Wu, M. Y. Liang, L. T. Chen, and L. Y. Yang, "Effect of surfactant on the formation and dissociation kinetic behavior of methane hydrate," *Chem. Eng. Sci.*, vol. 59, no. 21, pp. 4449–4455, 2004, doi: 10.1016/j.ces.2004.07.010.

[73] H. Ganji, M. Manteghian, K. Sadaghiani zadeh, M. R. Omidkhah, and H. Rahimi Mofrad, "Effect of different surfactants on methane hydrate formation rate, stability and storage capacity," *Fuel*, vol. 86, no. 3, pp. 434–441, 2007, doi: 10.1016/j.fuel.2006.07.032.